

A Molecular Gas Dynamics Study of Hypersonic Boundary Layer Second Mack Mode Instabilities

Mert Senkardesler, Irmak T. Karpuzcu, and Deborah A. Levin

University of Illinois, Urbana-Champaign, IL 61801, USA

Vassilis Theoflis

Technion - Israel Institute of Technology, Haifa 32000, Israel

(Dated: December 15, 2025)

Abstract

A flat-plate laminar boundary layer is simulated at Mach 6 and unit Reynolds number $Re_1 \sim 1.1 \times 10^7 \text{ m}^{-1}$ using the Direct Simulation Monte Carlo (DSMC) method to capture and analyze spontaneous second-mode instability growth. Power spectral density (PSD) analysis identifies dominant frequencies of 200–400 kHz, in line with linear stability theory (LST) predictions. Near-wall perturbations remain confined within the unstable regions known from linear theory. Dynamic Mode Decomposition (DMD) of unsteady flowfield snapshots reveals wave packets of spatially coherent modes having wavelengths and phase speeds characteristic of the acoustic second-mode; their growth and decay occurs exclusively within LST-predicted unstable bounds. Targeted interaction with these flow instabilities is demonstrated for an acoustic vibrating surface (AVS), where forcing at the unstable frequency of 300 kHz results in amplified waves downstream, while at the stable frequency of 500 kHz AVS-induced disturbances are damped. This further emphasizes the ability of the present kinetic simulations to capture and describe linear perturbations at high Reynolds numbers and suggests that DSMC will be a tool for understanding theoretically-founded control of laminar-turbulent transition in hypersonic boundary layers.

CONTENTS

I. Introduction	3
II. Overview of Numerical Approaches	8
III. Hypersonic Flat-Plate Boundary Layer	14
IV. Kinetic Characterization of Hypersonic Boundary-Layer Instabilities	19
A. Linear Stability Characterization of the Second Mack Mode	19
B. Spectral Characterization of Boundary Layer Instabilities	22
C. Spatial Analysis of Instability Waves via Dynamic Mode Decomposition (DMD)	29
V. Excitation of Second Mack Mode Instabilities by an Acoustic Vibrating Surface	36
VI. Conclusions	40
Acknowledgments	42
Appendix A: Derivation of Particle Speed Distribution for Moving Wall	43
References	46

I. INTRODUCTION

Hypersonic boundary-layer transition to turbulence governs thermal loads, aerodynamic drag, and vehicle performance. At subsonic and low-Mach number supersonic speeds, viscous Tollmien–Schlichting waves (the first mode) dominate. For Mach numbers greater than about four, an inviscid acoustic instability first identified by Mack (the second mode) prevails and governs the transition process in planar and axisymmetric high-speed boundary layer flows[1]. The boundary layer acts as a waveguide for this instability when a region of locally supersonic flow relative to the disturbance phase velocity traps acoustic waves between the surface and the sonic line [2]. The resulting resonance selectively amplifies high-frequency disturbances and drives rapid growth toward transition. Although the phenomenon of Mack mode instability has been well studied experimentally and computationally, there exists room for revisiting this instability using kinetic theory methods, as will be discussed shortly.

Experimental investigations have historically formed the bedrock of our understanding of high-speed boundary layer linear instability and laminar-turbulent-transition [3]. Seminal experiments by Stetson et al. [4, 5] on slender cones at Mach 8 provided the benchmark datasets that characterized the growth of second-mode waves and identified them as the dominant instability mechanism in high Mach number boundary layer flows. These and subsequent experiments favored conical geometries to ensure flow axial symmetry and study flow instability development in isolation from three-dimensional effects typical of finite-span flat plates, cones at an angle of attack and regions of flow inhomogeneity on flying vehicles. The physical development path for Mack mode instabilities and flow transition was canonically framed by Morkovin’s ”Path A” [6], which outlines receptivity, linear modal (exponential) perturbation amplification, and nonlinear breakdown as sequential stages preceding laminar-turbulent transition. To delay breakdown, the linear amplification stage is the primary focus, and linear stability theory (LST) supplies the theoretical basis for locally unstable frequencies, wavelengths, and spatial growth rates[7, 8]. To bridge linear stability theory with transition measurements, semi-empirical tools such as the e^N method and the Parabolized Stability Equations (PSE) [9] correlate the integrated local growth of the most unstable mode with transition onset. However, the predictive power of the e^N and the PSE method is limited because they both require assumed initial amplitudes that are facility dependent.

In comprehensive reviews, Schneider [10, 11] synthesized decades of ground- and flight-test data on cones, highlighting the persistent challenges posed by facility noise in conventional wind tunnels, which often leads to premature transition and ambiguously low transition Reynolds numbers compared to flight. Noisy tunnels typically report lower critical factors ($N \approx 5$ to 8) than quiet tunnels or flight ($N \approx 9$ to 11) [10–14]. Experimental and flight measurements, while invaluable, provide only a partial picture of second-mode dynamics, mainly due to the difficulty of providing the respective disturbance environments. Surface-pressure probes resolve localized wall disturbances [15], and Schlieren imaging visualizes density gradients [16], but neither technique yields a comprehensive spatio-temporal view of the unsteady flow field. Receptivity questions further compound the difficulty to provide a complete description of the laminar-turbulent transition scenario from its inception up to the location of the turbulent transition front(s) on the surface of a vehicle.

Direct numerical simulations (DNS) have contributed to complement experimentally gained instability and transition information in the continuum regime. However, the receptivity problem remains key to a complete description of laminar-turbulent transition: environmental disturbances such as freestream acoustic, entropic or vortical perturbations [17–21], wall vibrations, surface roughness, or particulates are proposed to set the disturbance amplitudes that the unstable flow subsequently amplifies [11, 22]. Since the ultimate transition location depends on the initial disturbance amplitudes, a truly predictive method must be based on a first-principles account of both receptivity and subsequent evolution [23]. This need is particularly pronounced in low-disturbance environments, such as high-altitude flight, where conventional receptivity sources are weak. Recent DNS efforts in this direction include the Mach 6–10 boundary layer studies that introduce targeted perturbations via freestream acoustic waves [24] or wall blowing–suction actuators [25] and follow the process through to laminar breakdown.

Focusing on the nose region of a conical flowfield, which is significant from a receptivity perspective, the sensitivity of second-mode growth to nose bluntness was established in early experiments [4], but the mechanism remained unresolved for decades, giving rise to the so-called "blunt-body paradox": increasing the leading-edge radius up to a point delays transition, while past a certain nose bluntness the transition front returns back toward the cone tip. Recent analyses of Paredes et al. [26, 27] proposed that non-modal perturbation growth plays a role, while work by Batista et al. [28] argued that the stronger, more de-

tached bow shock from a blunter nose creates a thick entropy layer. This layer weakens the near-wall density gradient that sustains the second-mode acoustic resonance and suppresses instability growth until the entropy layer is ingested by the boundary layer further downstream. The DNS study by Zhong and Ma [23] demonstrated that the physics of this near-nose region is further complicated by multi-stage receptivity, where freestream acoustic waves do not directly excite the second mode, even in regions where LST predicts it to be unstable. Instead, external disturbances first excite a stable first mode instability. This wave convects downstream until its wavenumber and phase velocity synchronize with the second mode, at which point efficient energy transfer occurs and rapid amplification begins. Regarding leading-edge effects, recent kinetic simulations further show that shock–shear-layer interaction near a cone tip can preferentially amplify non-axisymmetric instabilities, making this region a source of often-overlooked disturbances [29].

Due to its significance, receptivity at the leading edge region of a laminar boundary layer has received extensive theoretical attention across all speed regimes, invariably within the continuum framework [e.g. 30–32]. Addressing the same problem by DNS is rather challenging, on account of strong shocks and shock–boundary-layer and entropy-layer interactions, near-tip rarefaction and nonequilibrium effects. Controlled transition numerical experiments using DNS [24, 25, 33–35] have shed light on individual scenarios within the continuum limit. However, the leading edge region is also where rarefaction effects such as slip velocity and temperature jump are strong; such phenomena have been shown to stabilize second-mode instabilities while mildly destabilizing first-mode waves [36]. While slip velocity and temperature jump boundary conditions [37] may be incorporated in DNS, a kinetic, first-principles approach to the present problem can be employed, whereby rarefied gas phenomena are captured naturally, the flow evolves from collisional length scales, slip velocity and temperature jump are incorporated in the simulation without modeling and the internal structure of the shock layer formed ahead of the leading edge is fully resolved [38].

In the present effort, a kinetic approach to analyze hypersonic boundary layer instabilities is adopted using DSMC, a first-principles kinetic solver of the Boltzmann equation that naturally captures stochastic thermal fluctuations, velocity-slip and temperature-jump effects, shock-layer internal structure and shock–boundary-layer coupling inaccessible to continuum solvers [39]. DSMC has historically been used in rarefied, nonequilibrium regimes (including reacting chemistry) [40, 41], however, due to its massively parallelizable algorithm it is well

suited to present day high performance computers that allow one to capture continuum flows. In such regimes DSMC, which is inherently time-accurate, has been used to study shock-dominated flows and transition-relevant unsteadiness [42–44]. Here, we revisit compressible laminar flat plate boundary layer stability using kinetic theory at the to-date highest unit Reynolds number addressed in the literature, concretely two orders of magnitude higher than that in Klothakis et al. [45], with a three-fold objective: (1) assess the ability of DSMC to capture unstable Mack modes, (2) investigate the Mack mode in the receptivity region near the leading edge at lower Reynolds numbers predicted by linear stability theory and (3) understand and demonstrate the linear interaction with an acoustic vibrating surface. We compute second-mode instabilities in a Mach 6 boundary layer flow over a flat-plate portion $x \approx 35\text{--}100\text{ mm}$, $R \equiv \sqrt{Re} \approx 500\text{--}1150$, at $Kn \approx 0.05$, in the slip-flow regime. It will be shown that simulations capture spontaneously arising instabilities at the present Reynolds numbers and exhibit a higher-frequency spectrum in the range $F \approx 1.5 \times 10^{-4}\text{--}3.0 \times 10^{-4}$, consistent with LST predictions. The presently computed spectra complement those of Al Hasnine et al. [46], who obtained dominant frequencies of $F \approx 0.7 \times 10^{-4}\text{--}1.0 \times 10^{-4}$ created by particulate impingement further downstream at somewhat higher Reynolds numbers ($R \approx 1374\text{--}2517$).

The manuscript is organized as follows. Section II provides details about the numerical approaches, including the DSMC method and the data analysis techniques, used to compute the flowfield and characterize its instabilities. Specifically, the analysis of the stochastic, unsteady time-resolved flowfields is carried out using local Power Spectral Density (PSD) analysis for temporal characterization and global Dynamic Mode Decomposition (DMD) for spatio-temporal mode extraction and to compute N-factors for second-mode waves. The latter, which identifies multiple modes with unique frequencies and growth rates directly from snapshot data [47], has been demonstrated recently in the analysis of DSMC unsteady compressible ramp flows [48]. Here, DMD is applied to the full set of primitive variables. The method is shown to be especially valuable in the upstream receptivity region, since relatively wide band of unstable frequencies exists simultaneously, where the DMD decomposes the second-mode wave packet into components with distinct wavelengths, phase speeds, and growth behavior, providing a data-driven analogue to global instability analysis [49]. In Section III, the theoretical framework for the hypersonic flat-plate boundary layer is established using the compressible Blasius solution, which serves to validate the mean flow com-

puted in the simulations, and provide a guide for the precise placement of numerical probes. Section IV presents our primary findings on the spontaneously generated second-mode instabilities in the present kinetic simulations, detailing their spectral and spatio-temporal characteristics and comparing them against linear stability theory. After establishing the kinetic-theory based analysis methodology and characterizing the second mode instabilities in the baseline case, Section V investigates the targeted influence on the second-mode instability via an acoustic vibrating surface (AVS), assessing frequency-selective interactions with flow instabilities. Conclusions are offered in Section VI, while technical details on the derivation of the particle seed distribution on a moving wall are offered in the Appendix.

II. OVERVIEW OF NUMERICAL APPROACHES

Direct Simulation Monte Carlo (DSMC) is a well known, mature particle-kinetic stochastic method that provides reliable intrinsically unsteady numerical solutions of the Boltzmann equation of transport [50] when appropriate cell size, time step and number of particles are employed. The Boltzmann equation is the most general equation that describes the fluid motion allowing one to capture all non-equilibrium and rarefaction effects with the highest physical fidelity possible especially in flows where shocks are present. In DSMC, gas flows are simulated by tracking the motion and collisions of numerous representative particles, with macroscopic flowfield properties obtained by averaging the microscopic properties of particles within each computational cell.

While the vast majority of DSMC simulations are performed to model steady flows, the recent work of [44, 45, 51] shows its importance in modeling unsteady flows dominated by shock-shock and shock-boundary layer interactions. At the same time, use of kinetic methods offers insights into laminar flow instability that are inaccessible to classic continuum-equations based approaches [38, 45]. The current study, uses the DSMC method to model the flow over a hypersonic boundary layer, with Reynolds numbers up to $11.76 \times 10^6 \text{ m}^{-1}$ and a domain length of 120 mm. To the authors' best knowledge, this is the first time the DSMC has been used in this Reynolds number regime to time resolve and capture second-mode instabilities and their interactions with instabilities caused by an acoustic vibrating surface (AVS).

The 2D DSMC simulation parameters along with free-stream conditions used in this work are provided in Table I. To model gas particle collisions, the majorant frequency scheme[52] is utilized in the SMILE [53] DSMC solver. The viscosity-temperature dependence of the gas was accurately modeled using the Variable Hard Sphere (VHS) [50] model for molecular nitrogen at a reference temperature of 273 K, with molecular diameter and viscosity coefficient of $4.17 \times 10^{-10} \text{ m}$ and 0.255, respectively. Simulations were performed for a total of 600,000 timesteps with a timestep of 1 ns where the unsteady flow was allowed to evolve to steady state after 400,000 timesteps and then sampled an additional 200,000 time steps (0.2 ms) beyond steady state.

TABLE I: Freestream values and DSMC numerical parameters

Freestream Conditions	
Freestream pressure P_∞ (Pa)	828
Freestream temperature T_∞ (K)	50
Freestream Mach number	6.0
Reynolds number (m^{-1})	1.176×10^7
Mean free path λ (m)	6.148×10^{-7}
Number density (m^{-3})	1.2×10^{24}
Wall temperature (K)	300
DSMC Numerical Parameters	
Flow domain size (mm \times mm)	120×3
Simulation time step Δt (s)	1×10^{-9}
Sampled timesteps	200,000
Sampling cell size (m)	4×10^{-5}
Number of simulation particles	1.5×10^9

Figure 1 shows the elements and interconnections of the different computational tools that will be used to render the DSMC unsteady flow disturbances into spatially coherent modal structures observed in this work. In Figure 1 (a) a schematic of the flat plate boundary layer flow features and the probe locations and DMD window region, as well as the location of an acoustic vibrating surface (AVS) are shown. the presence of a leading-edge oblique shock that separates the freestream and post-shock inviscid region and the thin viscous boundary layer just above the surface can be observed, as expected in this well known hypersonic flow over a flat plate. The instabilities that are studied in this work are established in the viscous boundary layer and are most clearly observed in the shear layer at the edge of the boundary layer. In addition to observing and characterizing these instabilities in the unseeded DSMC free stream, a second type of simulation will be performed where an AVS, 1 mm in width, is placed on the surface at $x = 60$ mm to interact with the second-mode instabilities. We will refer to these two types of simulations as baseline and AVS cases, respectively. Note that the AVS case configuration permits the study of how unsteady boundary layer flow properties impact a targeted acoustic excitation generated by the AVS to selectively interact with expected second-mode frequencies of the developing second-mode instabilities.

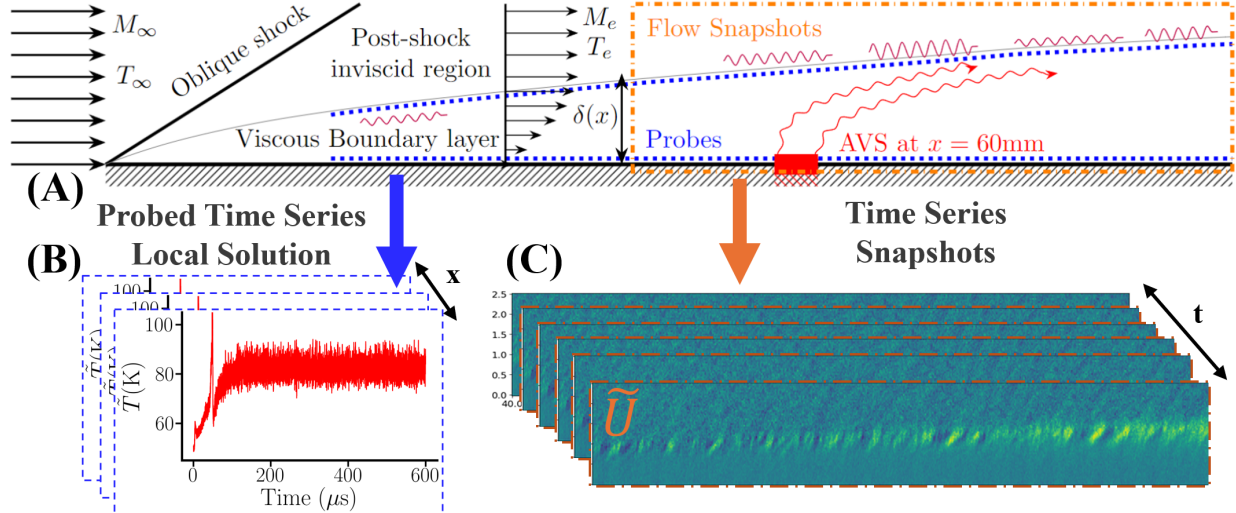


FIG. 1: Computational workflow: (a) Boundary layer flow and probes and AVS placement, (b) time-series probe data of power spectral density (PSD) spectral analysis of DSMC time-accurate temperature data, and (c) flowfield snapshots of fluctuating DSMC streamwise velocity to be used in modal decomposition.

DSMC simulation data for analyzing the boundary layer instabilities are acquired through two primary methods. First, unsteady flow data from individual DSMC cells at every timestep are sampled at probes locations positioned along the shear layer, where the wall-normal heights of the 180 probes are determined from the compressible boundary layer solution presented in Sec. III. This ensures that at each streamwise location the flow is probed at a height corresponding to consistent equivalent flow conditions according to the similarity solution. The study also includes another set of probes, placed along the wall-normal direction at $x = 60, 70$, and 90 mm that record how the disturbance amplitudes and frequency contents vary with distance from the wall. The flow was observed to reach steady state throughout the domain after 400,000 timesteps (0.4 ms). The locally probed data are decomposed into mean and unsteady components and then analyzed with power spectral density (PSD) analysis to identify dominant frequencies, as shown in Figure 1(b). In the freestream, the frequency spectrum was found to contain both thermal and DSMC noise, as expected since no artificial source perturbations were seeded in the DSMC simulation. However, in DSMC probe data from inside the boundary layer, discrete spectral peaks are observed, indicating that a mechanism different from the thermal, hydrodynamic source, amplifies disturbances at selected frequencies. As will be shown in Sec. IV B, these frequencies are consistent with second-mode instabilities.

While PSD provides a robust picture of local temporal behavior, it does not provide information on the spatial coherence of any unsteadiness that it captures. To address this aspect the method of snapshots is applied to snapshots of DSMC flowfield data that is analyzed using the general Dynamic Mode Decomposition (DMD) algorithm.[54] DMD, a data-driven technique, that does not require any prior assumptions about the expected instabilities, identifies spatially coherent modes associated with the DSMC unsteady flowfield, along with obtaining the respective frequencies of these modes, where one should expect to obtain frequencies similar to those from the PSD analysis.[54] This approach complements the localized PSD analysis because it further obtains the wave structures and spatial evolution of instabilities. In earlier work we investigated the use of data driven methods such as DMD to study the unsteadiness of high speed flows over several compression-expansion ramp geometries simulated with DSMC with large separation regions regions.[48] Here we provide a summary of the key elements of the method.

DMD represents a flow variable such as the streamwise velocity, $u(x, y, t)$, as a superposition of temporally harmonic contributions, each with a unique angular frequency ω_j and a complex spatial mode $\hat{u}_j(\mathbf{x}, \mathbf{y})$:

$$u(x, y, t) = \operatorname{Re} \left(\sum_j \hat{u}_j(\mathbf{x}, \mathbf{y}) e^{i\omega_j t} \right), \quad (1)$$

To relate these data-driven modes to classical wave parameters, we factor each spatial mode as

$$\hat{u}_j(\mathbf{x}, \mathbf{y}) = \hat{u}_j(y) e^{\sigma_j x} e^{i\alpha_j x}, \quad (2)$$

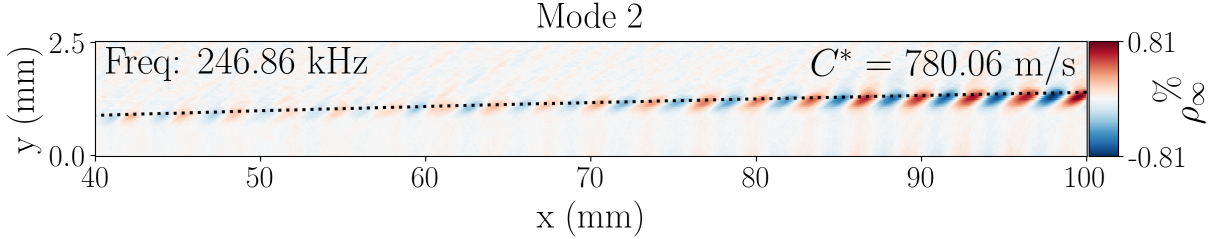
where $\hat{u}_j(y)$ denotes the wall-normal profile at the indicated location, α_j is the real streamwise wavenumber (wavelength $\lambda_j = 2\pi/\alpha_j$), and σ_j is the real spatial growth ($\sigma_j > 0$) or decay ($\sigma_j < 0$) rate. With this convention, the j th contribution to the instantaneous macroparameter field is

$$u_j(x, y, t) = \operatorname{Re} \left([\hat{u}_j(y) e^{\sigma_j x} e^{i\alpha_j x}] e^{i\omega_j t} \right), \quad (3)$$

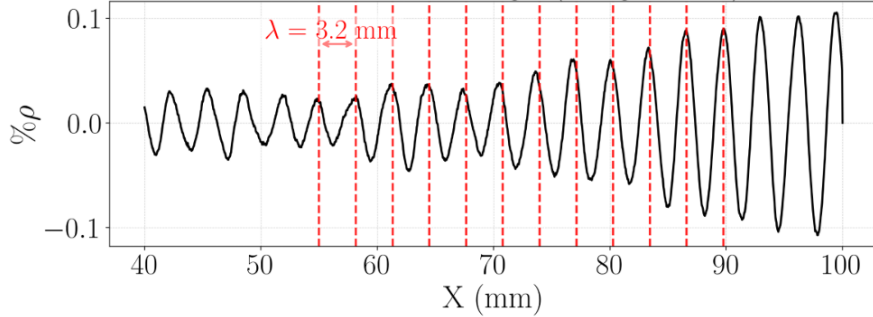
which is the standard LST normal-mode representation, written in terms of DMD outputs. Thus, DMD provides the global spatial mode $\hat{u}_j(\mathbf{x}, \mathbf{y})$, from which the quantities α_j , σ_j , and

$\hat{u}_j(y)$ may be extracted, enabling a direct connection to linear-stability interpretations. Figure 1(c) shows time accurate DSMC flowfield solution states of spatial domain size 1501×63 points, between $x = 40$ and $x = 100$ mm, that results in 6,000 time-accurate fields spanning the entire simulation progression. We note that the flow snapshots are time averaged over 100 DSMC timesteps ($0.1\mu\text{s}$) to reduce noise due to the finite number of DSMC simulated particles. These window snap shot parameters allow the resolution of second-mode instabilities anticipated in the 100–500 kHz range with a snapshot sampling frequency of 10 MHz (Nyquist limit of 5 MHz) sufficient for the target frequencies while effectively suppressing DSMC noise.

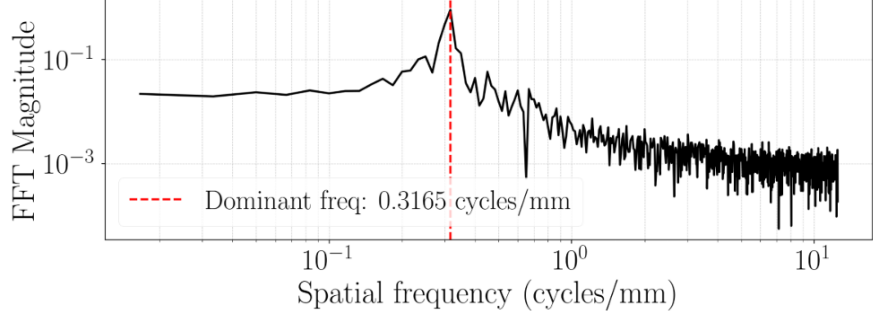
Once the DMD modes are obtained it is important to extract key wave properties, specifically, wavelength and phase speed from the spatial structures of the modes. An example of a DMD mode extracted from the unsteady density field that will be analyzed in Sec. IV C is shown in Fig. 2a. This mode, corresponding to a frequency of 247 kHz, clearly shows spatially coherent wave structures propagating along the shear layer. To quantitatively determine the wavelength of these structures, the amplitude of the captured waves in the DMD modes is extracted along the boundary-layer edge in the streamwise direction from $x = 40$ to 100 mm. This process yields a one-dimensional signal, $u(x)$, representing the spatial oscillation of the mode, as depicted in Fig. 2b



(a) Density perturbation mode at 247 kHz showing spatial wave structures and boundary-layer thickness (dotted) from the compressible boundary layer solution (Sec. III).



(b) Spatial oscillation profile along $x = 40\text{--}100 \text{ mm}$ used for wavelength extraction.



(c) Corresponding Fourier spectrum.

FIG. 2: Extraction of wavelengths of traveling waves from DMD modes.

To find the dominant spatial frequency, a Fast Fourier Transform (FFT) is applied to this signal $u(x)$ thereby decomposing the signal from the spatial domain into the wavenumber domain, *i.e.*,

$$\hat{u}(k_x) = \mathcal{F}\{u(x)\} = \int u(x) e^{-ik_x x} dx \quad (4)$$

where k_x is the streamwise wavenumber. The resulting power spectrum, $|\hat{u}(k_x)|^2$, exhibits a distinct peak at the dominant wavenumber, $k_{x,\text{dom}}$, as illustrated in Fig. 2c. The wavelength λ of the disturbance is then calculated from this dominant wavenumber as,

$$\lambda = \frac{2\pi}{k_{x,\text{dom}}} \quad (5)$$

This procedure provides a robust method for extracting a near-constant wavelength from the spatially-resolved DMD mode. Once the wavelength λ is determined, the dimensional phase speed c^* of the traveling wave can be calculated using the DMD-identified temporal frequency w^* :

$$c^* = \lambda \cdot w^* \quad (6)$$

where w^* is the frequency (e.g., 246.9 kHz) and λ is the wavelength. This approach provides a complete characterization of the perturbation waves in both time and space. For comparison with stability theory, this dimensional phase speed is non-dimensionalized using the boundary layer edge velocity, $U_e^* \approx 858 \text{ m/s}$:

$$c = \frac{c^*}{U_e^*} \quad (7)$$

where c is the dimensionless phase speed taken as 0.91 because, as will be shown in Sec. IV C, the modes that are obtained have a phase speed between 0.9 - 0.93. This fixed value facilitates transformations between spatial wavenumber and temporal frequency, which is necessary for consistent comparisons between the simulation results and linear stability theory.

III. HYPERSONIC FLAT-PLATE BOUNDARY LAYER

To study the behavior of boundary layer instabilities and to determine specific locations for DSMC probes, the boundary layer general structure must be known. In this section we start with the well known compressible Blasius solution modified to account for slip. Using the boundary layer thickness as the characteristic length, the Knudsen number Kn is given by [55]:

$$Kn = \frac{M_e}{\sqrt{\text{Re}}} \quad (8)$$

which in this work gives $Kn \approx \frac{5.85}{\sqrt{11760}} \approx 0.05$, assuming the free stream conditions given in Table I, $M_e = 5.85$ at the boundary layer edge, a boundary layer thickness, $\delta = 1 \text{ mm}$, and a Reynolds number $\text{Re} = 11,760$. This value indicates that the flow falls well within the

slip flow regime ($0.01 \leq Kn \leq 0.1$) meaning that gas molecules exhibit a finite tangential velocity relative to the surface. The relaxation of the no-slip condition fundamentally alters the boundary layer structure by reducing the shear stress exerted by the body on the flow, *i.e.*, velocity slip leads to weaker near-wall velocity and temperature gradients. As shown in previous DSMC simulations,[45] this results in a more stable boundary layer with increased damping of flow perturbations compared to predictions from no-slip, continuum approaches.

The magnitude of the slip velocity is given by:

$$u_{\text{slip}} = \frac{2 - \sigma_v}{\sigma_v} \lambda \frac{\partial u}{\partial y} + \frac{3}{4} \frac{\mu}{\rho T} \frac{\partial T}{\partial x} \quad (9)$$

where σ_v is the tangential momentum accommodation coefficient (taken as 1.0 in the present DSMC simulations), λ is the mean free path, u is the velocity in the streamwise direction, and y is the wall-normal direction. Equation 9 can be used to modify the no-slip boundary condition in continuum simulations such as the compressible flat plate flow solutions, but is not needed in DSMC as it is a natural outcome of the kinetic simulation.

Figure 3 shows profiles of slip velocity and temperature jump obtained using Eq. 9 and the DSMC simulation. It can be seen in the figure that near the leading edge, slip velocities reach approximately 60 m/s, accompanied by steep pressure gradients, but, these effects diminish downstream, with slip velocity falling to around 10 m/s by 15 mm. It can also be seen that the temperature jump in the developed region of the simulation is only on the order of 1 K and therefore will be neglected.

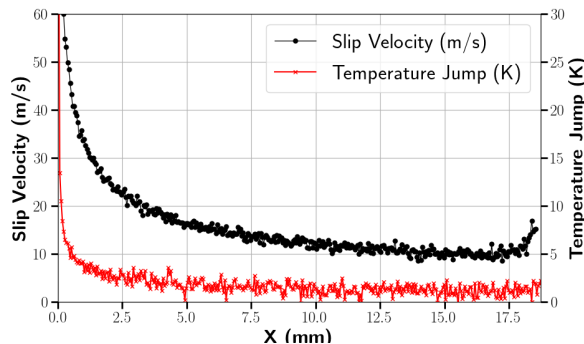


FIG. 3: Slip velocity and temperature jump profiles along the surface from the DSMC solution.

The theoretical solution for compressible boundary-layer flow over a flat plate can now

be obtained using the Crocco method [56]. This theory assumes the gas is calorically perfect with a constant specific heat capacity while accounting for temperature-dependent viscosity and thermal conductivity. For compressible flow over a flat plate, a self-similar solution within the boundary layer can be obtained through an appropriate transformation of the independent variables. In the transformed plane (ξ, η) , the velocity profile becomes independent of ξ and can be expressed as $u = u(\eta)$. The independent variables in the transformed space (ξ, η) relate to those in the physical space (x, y) by:

$$\xi = \int_0^x \rho_e u_e \mu_e dx \quad \eta = \frac{u_e}{\sqrt{2\xi}} \int_0^y \rho dy \quad (10)$$

The governing equations in the transformed plane (ξ, η) are given by:

$$(C f'') + f f'' = 0 \quad (11)$$

$$\left(\frac{C}{Pr} g' \right)' + C \frac{u_e^2}{h_e} (f'')^2 = 0 \quad (12)$$

where $C = \frac{\mu}{\rho_e u_e \mu_e}$, ρ and μ are the density and dynamic viscosity, respectively, and the subscript e denotes values at the edge of the boundary layer. The Prandtl number $Pr = \frac{\mu c_p}{k}$, where c_p is the specific heat capacity at constant pressure, and k is the thermal conductivity. The power law viscosity model is used in this study, given by $\mu = \mu_{\text{ref}} \left(\frac{T}{T_0} \right)^\omega$ where μ_{ref} is the reference viscosity, T is the temperature, T_0 is the reference temperature, and ω is the exponent. In this study, $\omega = 0.74$ for molecular nitrogen [56]. The solution to the boundary-layer equations requires appropriate boundary conditions at the wall ($\eta = 0$). For flow with velocity slip at the wall, these boundary conditions are:

$$f(0) = 0, \quad f'(0) = u_{\text{slip}}, \quad g(0) = g_w \quad \text{for an isothermal wall} \quad (13)$$

By solving these transformed equations with the specified boundary conditions, we obtain the variations of velocity and enthalpy across the boundary layer, leading to the self-similar solution for the compressible boundary layer over a flat plate. The dependent variables of Eqs. (11) and (12) can be obtained from the transformed variables as:

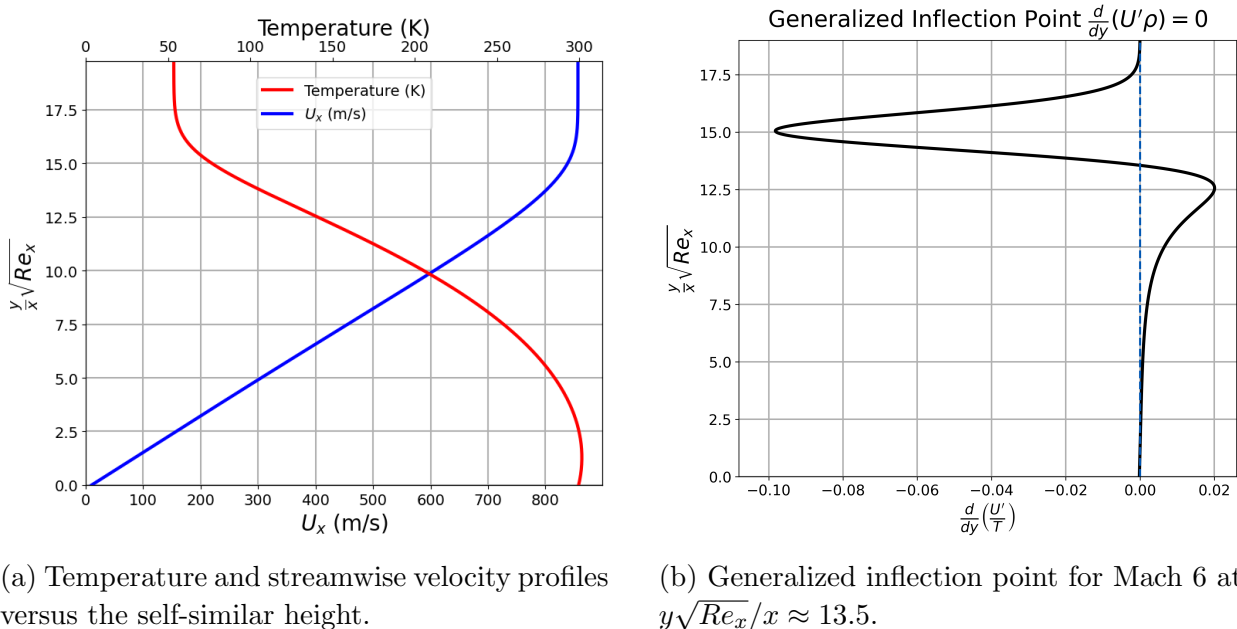
$$u = f' U_e^* \quad \text{and} \quad h = h_e g \quad (14)$$

where U_e^* denotes the dimensional freestream velocity at the boundary layer edge.

The compressible Blasius boundary layer solution provides the baseline boundary-layer profiles, expressed in terms of the similarity coordinate η and the functions $f(\eta)$ and $g(\eta)$. The obtained solution is shown in Fig. 4a, which illustrates the non-monotonic temperature profile characteristic of hypersonic boundary layers. The solution also exhibits a generalized inflection point, defined as the location where

$$\frac{d}{dy} \left(\rho \frac{dU}{dy} \right) \Big|_{y=y_g} = - \frac{U_e}{T_e} \cdot \frac{f'''g - f''g'}{\sqrt{2}g^5} = 0 \quad (15)$$

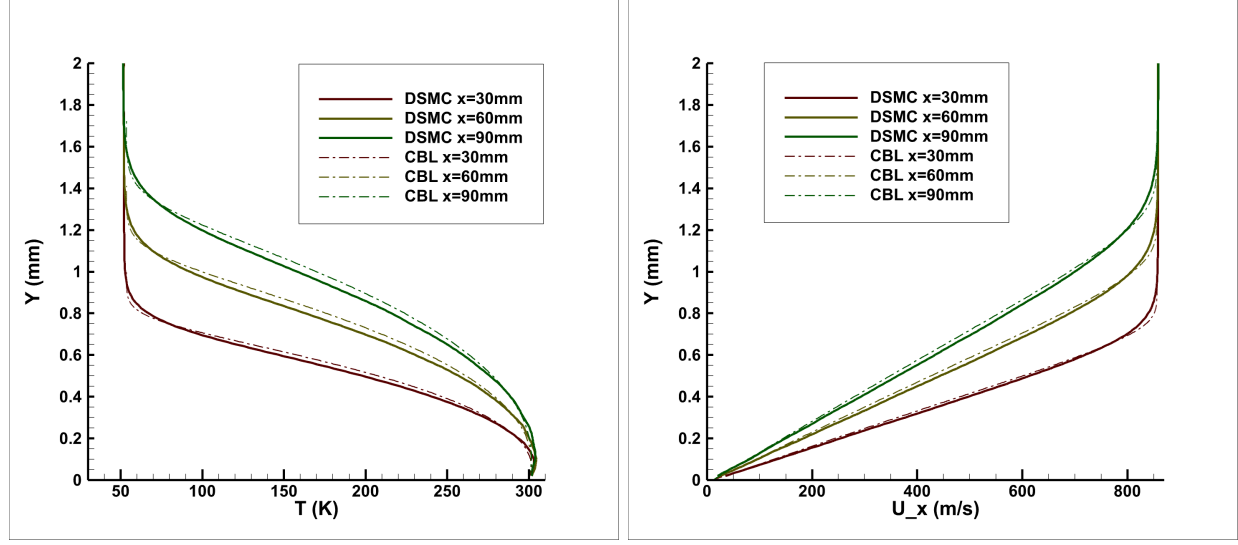
This point indicates the necessary condition for the existence of inviscid instabilities, as it satisfies a sufficient condition for Rayleigh's inflection-point theorem in compressible flows. As shown in Fig. 4b, the generalized inflection point occurs height of $y\sqrt{Re_x}/x \approx 13.5$.



(a) Temperature and streamwise velocity profiles versus the self-similar height.

(b) Generalized inflection point for Mach 6 at $y\sqrt{Re_x}/x \approx 13.5$.

FIG. 4: Compressible Blasius boundary-layer profiles and generalized inflection point.



(a) Temperature profiles.

(b) Velocity profiles.

FIG. 5: Comparison of DSMC results with the compressible Blasius solution at Mach 5.85, freestream temperature 52 K, freestream velocity 858 m/s, Prandtl number 0.72, and wall temperature 300 K.

Comparison of dimensional velocity and temperature profiles predicted by the compressible Blasius solution with DSMC results presented in Fig. 5 show excellent agreement, confirming the use of the compressible Blasius equations to help select meaningful probe locations for DSMC simulations at this Reynolds number. More specifically, the boundary layer equations are used to determine the would be boundary-layer thickness δ_{99} along the streamwise direction x , as shown in Fig. 6. The δ_{99} values will be used to efficiently place virtual probes in the DSMC simulations near the edge of the boundary layer where second-mode instabilities exhibit peak amplitudes.

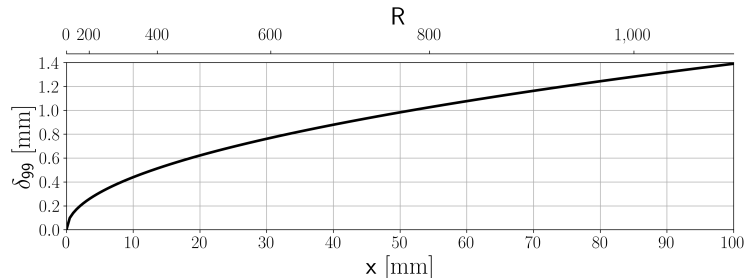


FIG. 6: Boundary-layer thickness profile obtained from the compressible Blasius equations as a function of distance and dimensionless streamwise coordinate for the conditions specified in Figure 5.

IV. KINETIC CHARACTERIZATION OF HYPERSONIC BOUNDARY-LAYER INSTABILITIES

In hypersonic boundary layers, instabilities differ significantly from those in subsonic or low-supersonic flows, where Tollmien–Schlichting (T-S) waves, also known as the first or vorticity mode, dominate transition. At moderate Mach numbers ($M_e \leq 3$), T-S waves persist as the primary instability, driven by viscous effects. However, above Mach 4, and particularly at the Mach 6 conditions of this study, the first acoustic mode, referred to as the second mode, becomes the dominant instability, exhibiting significantly larger amplification rates [1, 57]. The second mode develops in regions of the boundary layer where the local flow is supersonic relative to the wave's phase speed. This condition, $M_c = (U - c_{ph})/\sqrt{T} > 1$, creates a waveguide between the wall and the sonic line ($M_c = 1$). This waveguide traps and reflects acoustic energy, and disturbances with frequencies that match the resonant characteristics of this guide are selectively and rapidly amplified. This powerful acoustic resonance mechanism explains the dominance of the second mode in hypersonic flows and accounts for the strongly amplified frequencies observed in the 100–500 kHz range in this DSMC study, as we discuss below.

A. Linear Stability Characterization of the Second Mack Mode

Linear stability theory for 2D instabilities postulates that the evolution of unsteady macroparameters can be written as

$$\tilde{u}(x, y, t) = \hat{u}(y) \exp \left[\int (-\alpha_i + i\alpha_r) dx - i \omega t \right], \quad (16)$$

where the complex streamwise wavenumber $\alpha = \alpha_r + i\alpha_i$ governs the spatial characteristics of disturbances in hypersonic boundary layers. The real component, α_r , determines the spatial wavelength of the disturbance through $\lambda = 2\pi/\alpha_r$, defining the streamwise periodicity of the perturbation waves. The imaginary component, α_i , controls the spatial growth or decay rate, where the local amplification rate is given by

$$\frac{1}{|\tilde{u}|} \frac{d|\tilde{u}|}{dx} = -\alpha_i. \quad (17)$$

A positive $-\alpha_i > 0$ indicates exponential growth of the perturbation amplitude as it propagates downstream, characteristic of convectively unstable modes, while $-\alpha_i < 0$ signifies damping, and $-\alpha_i = 0$ marks neutral stability.

Using LST, Ozgen et al. [58] recently obtained neutral stability curves describing the spatial and frequency dependence of the second Mack mode based on compressible boundary layer flows of Mach numbers from 2 -10 over a flat plate. This work provides a rigorous study of neutral stability curves verified by zero neutral decay rates. To enable comparison between DSMC results and the neutral stability curves, dimensional variables are converted into dimensionless forms consistent with boundary-layer stability theory. The dimensionless streamwise coordinate is defined as:

$$R = \sqrt{\frac{U_e^* x^*}{\nu^*}} = \sqrt{Re}, \quad L^* = \sqrt{\frac{\nu^* x^*}{U_e^*}}, \quad (18)$$

where U_e^* is the local velocity at the boundary-layer edge, x^* is the dimensional distance from the leading edge, ν^* is the kinematic viscosity, and Re is the Reynolds number based on x^* . The dimensionless angular frequency ω is related to its dimensional counterpart ω^* (in kHz) by:

$$\omega = \frac{2\pi\omega^* L^*}{U_e^*}, \quad F = \frac{\omega}{R} \quad (19)$$

incorporating the local length scale L^* and edge velocity U_e^* . The dimensionless wavenumber α is then defined as:

$$\alpha = \frac{\omega}{c}, \quad (20)$$

where $c = c^*/U_e^*$ is the dimensionless phase speed, with $c^* \approx 0.91U_e^*$ reflecting typical second-mode wave speeds at Mach 6, as determined from DSMC simulations. These transformations enable direct comparisons between the theoretical stability curves (expressed in α , ω , and R) and DSMC-derived results (in kHz and mm), providing a consistent framework to assess the onset and growth of second-mode instabilities.

Figure 7 allows us to convert dimensional results from the DSMC simulation to the dimensionless wavenumber α_r from Ozgen's results to dimensional frequency ω^* . This is achieved by rearranging the definition of the dimensionless wavenumber from Eq. (20) combined with the definitions for dimensionless frequency (Eq. (19)) and phase speed. The transformation relies on a phase speed $c^* \approx 0.91U_e^*$, with $U_e = 858 \text{ m s}^{-1}$ from our freestream

conditions, as mentioned earlier. In Fig. 7, the neutral curves derived from Ozgen's dimensionless analysis are transformed and re-expressed as ω^* (kHz) versus x (mm), incorporating $\nu^* = 7.313 \times 10^{-5} \text{ m}^2/\text{s}$ and the transformation $\omega^* = \alpha_r c^* / (2\pi R \sqrt{\nu^*/x^*})$. Consistent with Eq. 17, disturbances with frequencies and streamwise positions falling within the enclosed unstable regions experience spatial amplification. The outer boundary of each enclosed region corresponds to $-\alpha_i = 0$, marking neutral waves. Inside these regions, where $-\alpha_i > 0$, perturbations exhibit exponential spatial growth as they propagate downstream, defining a convectively unstable zone until they exit, where $-\alpha_i \leq 0$ indicates damping or neutral stability.

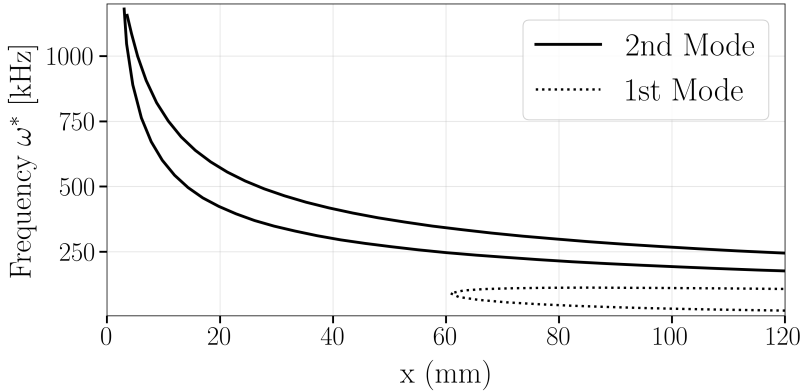


FIG. 7: Neutral stability curves based on the neutral stability curves of Figure 3e from the work of Ozgen et al. [58]. The figure takes his results and re-expresses the neutral stability curves in dimensional frequency (ω^*) versus streamwise position, transformed using the simulation parameters from the present study.

Finally, the well known N -factor is a key metric for assessing transition by the total amplification caused by the growth of perturbations and is defined as the integral of the growth rate over the unstable region,

$$N(x, F) = \int_{x_0}^x -\alpha_i(x', y_M) dx', \quad (21)$$

where y_M is the wall-normal location of maximum amplification. A higher N -factor indicates greater amplification, with critical values for transition often cited in the range of 9 to 11, depending on flow conditions.[12] In this work we will use the instabilities that arise naturally from the DSMC simulations to model the N -factor obtained from the DMD computed amplitudes. As is typical, the the N -factor will be obtained by normalizing the perturbation amplitude A at a given streamwise position x by its initial amplitude A_0 at the point where

amplification begins, x_0 ,

$$N(x, F) = \ln \left(\frac{A(x)}{A_0} \right) \quad (22)$$

to provide a direct measurement of the amplification factor, e^N .

B. Spectral Characterization of Boundary Layer Instabilities

With the boundary layer spatial features defined and the dimensional representation of neutral stability curves we analyze the spectral content of instabilities predicted by the DSMC kinetic approach. As shown in Fig. 1, Power Spectral Density (PSD) analysis is key in quantifying the frequency content of the unsteady DSMC data, *i.e.*, the power distribution across frequency bands. The PSDs are computed using Welch’s method [59] implemented in SciPy’s signal processing module [60]. The analysis used a sampling frequency of 1 GHz (corresponding to the 1 ns DSMC timestep) applied to the statistically steady portion of the DSMC data ($t_{\text{start}} = 400,000$ to $N = 600,000$ timesteps). The segment length was set to two-thirds of this steady-state data at 133,333 samples per segment. A Hann window was applied with 50% overlap between segments.

Figure 8a and 8b show the time series temperature data recorded over 600,000 DSMC timesteps at $x = 35$ and 90 mm. Initial transients die out after approximately 400,000 timesteps (600 μ s), after which the flow attains a statistically steady mean state. Qualitatively, it can be observed that there exists a stark difference in the unsteadiness of the captured signal in the freestream versus the boundary layer. The converged flow state is then analyzed via PSD as shown in Figs. 8c and 8d. The first observation is that well-defined spectral peaks are seen at both locations, which is even more clear when compared to the flat spectral response of the freestream that is relatively free of disturbances. Secondly, the spectral peaks from these two different locations are at different frequencies. PSD analysis reveals distinct frequencies that evolve with streamwise coordinate: at $x = 35$ mm, a pronounced peak emerges at approximately 440 kHz (Fig. 8c), while by $x = 90$ mm the dominant peak shifts to 280 kHz (Fig. 8d).

These PSD results show that the frequencies observed are consistent with the commonly observed Mack’s second-mode instabilities[1], however, to better relate to the neutral stability curves, the DSMC flow is probed along a continuous set of points in the streamwise

direction to allow PSD analyses at each point, as shown in Fig. 8e. It can be seen that frequencies outside the neutral stability curve of Ozgen *et al.*[58]) are damped by the flow, while those within the unstable region, between 440 to 280 kHz peaks corresponding to Reynolds number R values of 640 and 1,026 at streamwise locations of $x = 35$ and 90 mm are selectively amplified, driven by local flow instability. Note that this range is different from most second mode DNS studies that are able to capture the later stages of amplification up to the point of transition. An example is the work of Gai and Cao [61] which employs a 1-meter plate model to analyze thermal effects on transition far downstream, but does impose source perturbations in the free stream to excite second-mode waves. Our kinetic simulation in the region closer to the leading edge complements those studies and produces frequencies consistent with the high-frequency portion of the neutral stability curve for Mach 6 [58, 61] without any imposition of free stream disturbances.

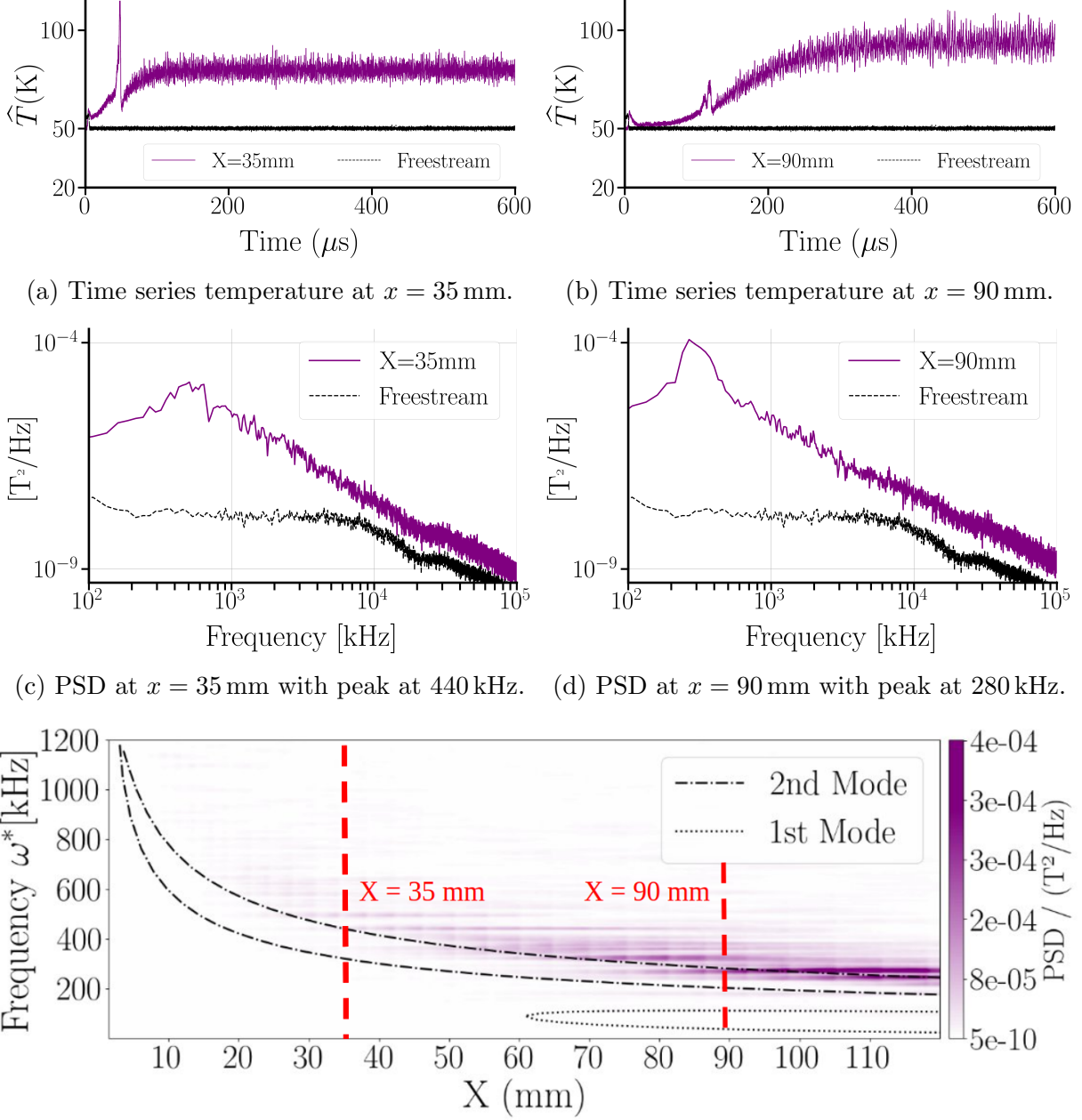


FIG. 8: Unsteady signals and spectra at two streamwise locations and spatial spectra along the boundary-layer edge.

The temporal dimensional results of the observed perturbations derived from the DSMC simulations can be transformed into a dimensionless spatial representation using Reynolds number, R and wavenumber, α , based on Eqs. 18 - 20. This transformation employs the freestream parameters values of $U_e = 858$ m/s, $c = 0.91$, and $\nu^* = 7.313 \times 10^{-5}$ m²/s

to allow us to convert time-domain frequencies into the more commonly used spatial definition counterparts. Figure 9 thus obtained shows the resulting power PSDs for pressure, temperature, and x-velocity in R-F space, computed from probes positioned at two heights within the boundary layer. One set of probes is strategically placed along the shear layer, defined as the wall-normal location where the velocity reaches 99% of U_e (approximately the boundary-layer edge), to capture convecting second-mode waves and the second set is positioned at a constant height of 0.3 mm above the wall, where the bulk flow velocity drops significantly to a subsonic value ($M < 1$) and pressure perturbations are expected to be more prevalent. The figure shows that near the wall, the dominant frequency ranges of perturbations lie strictly within the neutral curve [see Figs. 9a, 9c, and 9e]. This confinement to the locally unstable region indicates that disturbances in this vicinity are governed by local instability mechanisms, where frequencies within the neutral curve are selectively amplified.

In contrast, locations along the shear layer reveal a different behavior: the most dominant frequencies are observed outside the neutral curve, particularly downstream of the region where amplification occurs as depicted in Figs. 9b and 9d. Specifically, these dominant frequencies occur just outside the neutral curve in the downstream region, beyond the upper limit of the neutral stability boundary. This indicates that the observed waves were amplified while they were inside the neutral curve unstable region and we capture their peak amplitudes at or near the upper boundary of the neutral curve before they are convected further downstream (Figs. 9b and 9d). However, it should also be noted that streamwise velocity perturbations shown in Fig. 9f do not have the same behavior as the disturbances in Figs. 9b and 9d, even though they are taken at the boundary-layer edge. Instead, this implies that these perturbations are purely due to local instability mechanisms.

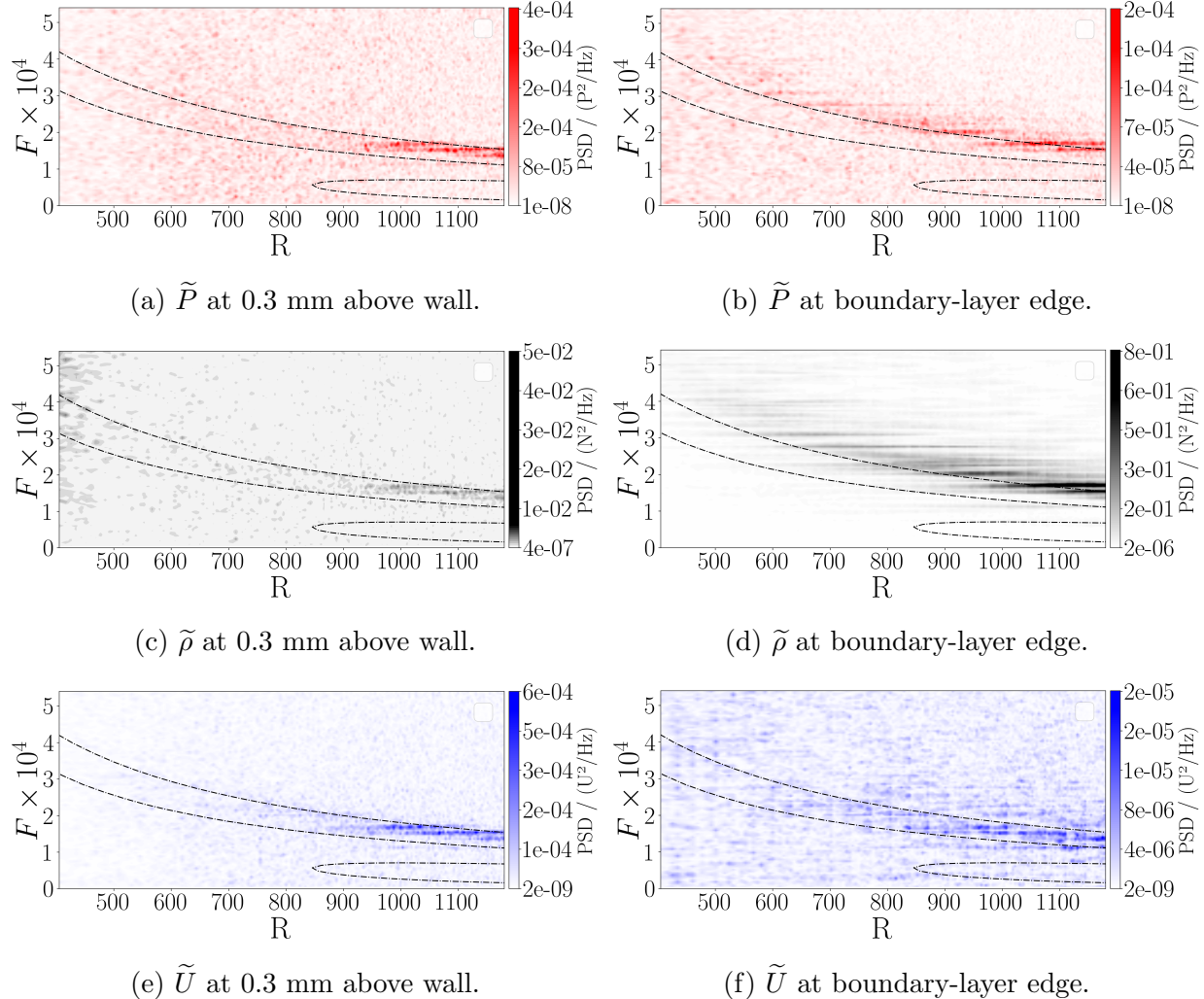


FIG. 9: PSD's of flow perturbations in R - F space (Eq. 19), comparing wall-normal locations at 0.3 mm above the wall (left column) and along the boundary-layer edge (right column). Black dashed lines represent the neutral stability curve boundaries from LST predictions [58].

After analyzing perturbation spectra at various wall-normal positions, it is evident that disturbances exhibit distinct behaviors across the boundary layer in the wall-normal direction. To explore this further, two specific streamwise stations at $x = 60$ and 90 mm were selected for a detailed PSD-based profile study at the locations shown in Figure 1 (a). Figure 10 presents the PSD distributions for pressure (\tilde{P}), density ($\tilde{\rho}$), temperature (\tilde{T}), and streamwise velocity (\tilde{U}) as functions of frequency and wall-normal coordinate, where the upper and lower bounds for the frequencies[58] in the locally unstable region are overlaid with black dashed lines, and heights corresponding to the inflection point and the boundary layer height are shown as blue and red vertical lines, respectively.

It can be seen in Figs. 10a and 10b that pressure fluctuations are most dominant near the surface and lie within the locally unstable frequency band. The same behavior is captured for streamwise velocity perturbations (Figs. 10c and 10d), indicating that amplification of \tilde{U} and \tilde{P} is governed by local instability characteristics of the boundary layer.

A different observation is made for density fluctuations, shown in Figs. 10e and 10f, where at a given streamwise location perturbations are most dominant along the boundary-layer edge and have frequency spectra grouped near the upper limit of the locally unstable band. This is not due to larger local amplification at higher frequencies; rather, it reflects upstream-originating unstable frequencies that convect to the measurement location. At any given streamwise position, these edge perturbations are an accumulation of upstream disturbances initiated by local instabilities. PSD spectra for temperature fluctuations are given in Figs. 10g and 10h, where the primary peak is near the boundary-layer edge with grouped frequencies near the upper bound. A secondary, much fainter, near-wall signal is also present and lies within the locally unstable band.

Overall, the relative wall-normal positions at which perturbations in each flow variable peak align with the amplitude functions predicted by Klothakis et al.[45] for a similar Mach number. The present study extends these by demonstrating that not only do the perturbation amplitude profiles differ among the flow variables, but the observed frequencies of these perturbations at any given streamwise location also vary, depending on whether they are dictated by local instabilities or spatially convected phenomena. The frequencies measured near the surface are not necessarily the frequencies of the instability that establish themselves at the edge of the boundary layer, at that streamwise location. This means that any controlled interaction of an instability at the boundary layer edge should ideally be targeted at an upstream location that would quench local instabilities before they accumulate downstream.

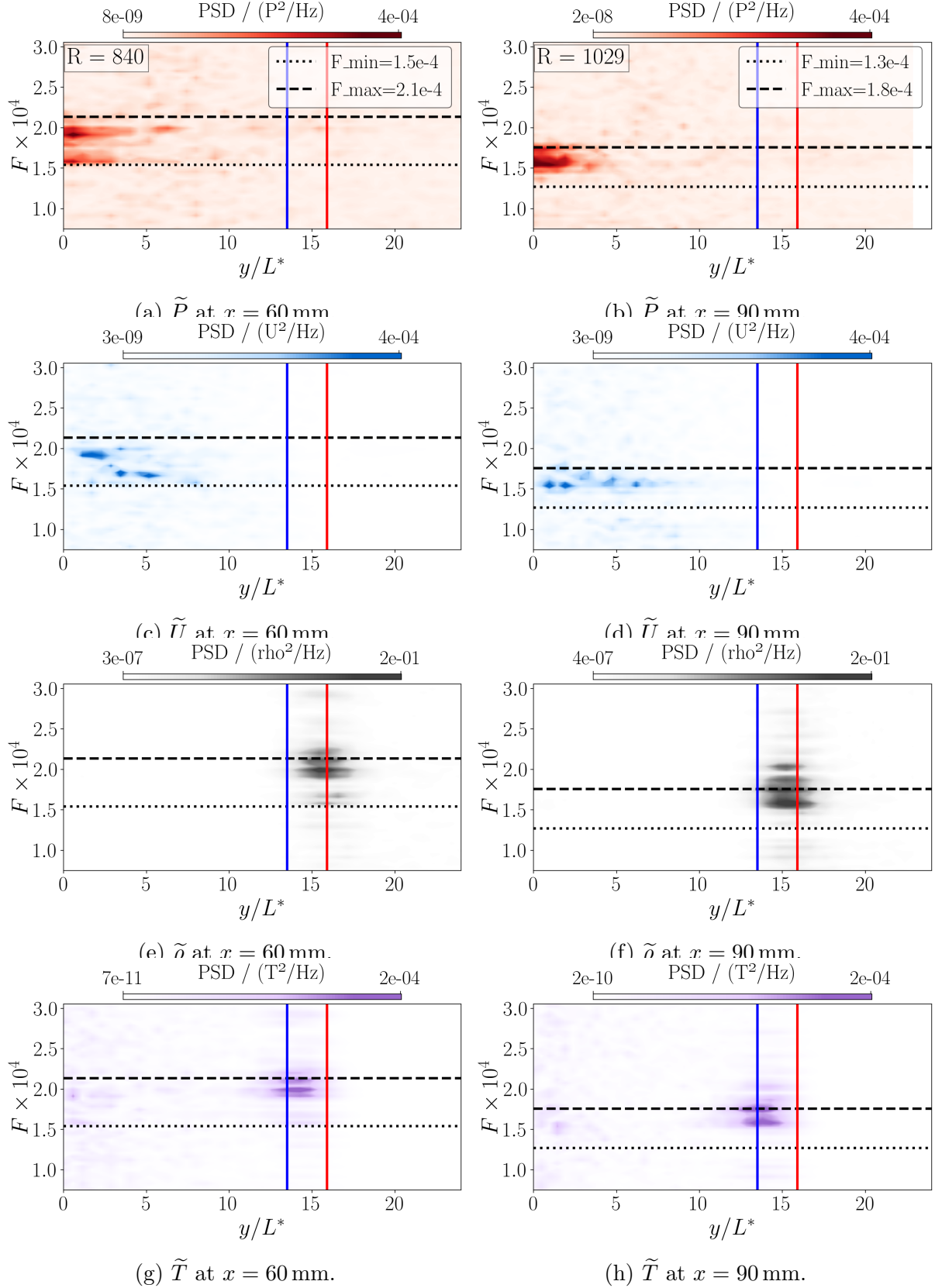


FIG. 10: PSD disturbance profiles for pressure, density, temperature, and streamwise velocity at two streamwise stations. Each panel shows PSD versus frequency and wall-normal coordinate y/L^* . Dashed horizontal lines indicate LST-predicted unstable frequency bands (Ozgen et al. [58]); red and blue vertical lines mark the boundary-layer height and generalized inflection point from the compressible Blasius solution.

C. Spatial Analysis of Instability Waves via Dynamic Mode Decomposition (DMD)

While the local PSD analysis described in Section IV B effectively identifies the frequencies of second-mode disturbances at discrete points, it does not leverage the fact that these instabilities inherently exhibit spatial coherence due to their wave-like propagation within the flow. Since these locally unstable frequencies are convected and accumulated as they propagate downstream, one should expect them to manifest as spatially coherent structures, particularly in the streamwise direction. This implies that, rather than analyzing local temporal unsteadiness everywhere in the domain and then building a global flowfield-wide understanding of the underlying physics from those local insights, we can instead impose a spatial coherence condition with unsteadiness that the actual flowfield possesses by solving for the DMD coherent spatial modes that emerge from time-series snapshots of DSMC data of the entire domain. From these modes, we can recapture their temporal frequencies as the final step, which should align with those identified in the local analyses discussed in the previous subsection. This approach imposes an additional constraint that focusses specifically on spatially coherent instabilities. For convective instabilities such as Mack's second mode, while local spectral methods such as PSD analysis can detect unsteadiness nearly everywhere, not all local instabilities will exhibit this spatial coherence, a distinguishing feature of the convective mechanisms under consideration.

Figure 11 shows the spectrum of the 11 most energetic modes normalized by the most dominant mode of the DSMC predicted flow over a flat plate. It can be seen that the dominant modes cluster between 200–400 kHz, consistent with the frequency range of second-mode instabilities identified in the PSD analysis (Fig. 8e). We retained 30 modes in the DMD analysis; due to complex-conjugate pairing, this yields 15 distinct frequencies, a number sufficient to resolve the dominant instability mechanisms while filtering numerical noise.

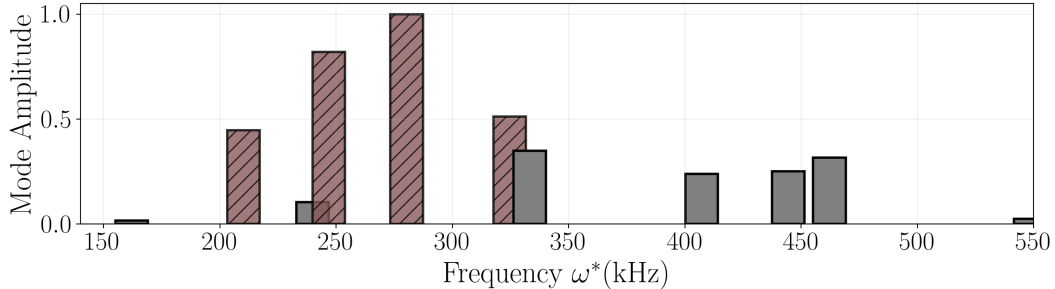


FIG. 11: Frequency spectrum of DMD modes showing normalized modal amplitudes. The amplitudes are scaled relative to the most dominant mode, with the top four energetic modes indicated by crosshatching.

The first four modes with the greatest amplitudes (shown with cross hatching in Fig. 11) correspond to frequencies of 280, 247, 325, and 210 kHz, in order of decreasing amplitude. Their spatial DMD mode shapes are presented in Figs. 12a–12d. Note that each mode displays coherent wave patterns with well-defined wavelengths and phase speeds (as defined in Sec. II) that differ from the bulk flow velocity, *i.e.*, 790 versus 858 m/s, a distinction that suggests that the modal structures are not artifacts of convected noise. Furthermore, this difference in propagation speed indicates that these second-mode disturbances are not purely convected with the bulk flow velocity but are acoustic in nature. As shown in Figure 12, the DMD analysis successfully isolates the spatially coherent wave structures of the most energetic modes, each associated with a distinct frequency. These modes all display density perturbations concentrated near the boundary-layer edge (dashed line) with a nearly constant wavelength along their streamwise evolution, ranging from 2.40 to 3.75 mm. A key physical characteristic confirming their identity as second-mode waves is that their wavelengths are approximately twice the local boundary-layer thickness.

The ability of DMD to resolve these individual wave structures is particularly valuable in the upstream region responsible for the initial instability development analyzed here. In this region, a broad spectrum of frequencies is simultaneously unstable, each with a relatively low amplification rate. This contrasts with analyses of downstream, more developed flowfields, where convective instabilities typically lead to the dominance of a narrow band of frequencies. Recent applications of DMD-based methods to experimental Schlieren data have successfully extracted the dominant second-mode wavepacket structure [62], but inherently focus on the later stages of growth where a single frequency has emerged. The present study leverages DMD’s capabilities in a different manner: by analyzing the spectrally rich upstream region, it

decomposes the second-mode wave system into its constituent wave components, as shown in the figure, revealing the variety of wavelengths and frequencies that contribute to the *initial* instability.

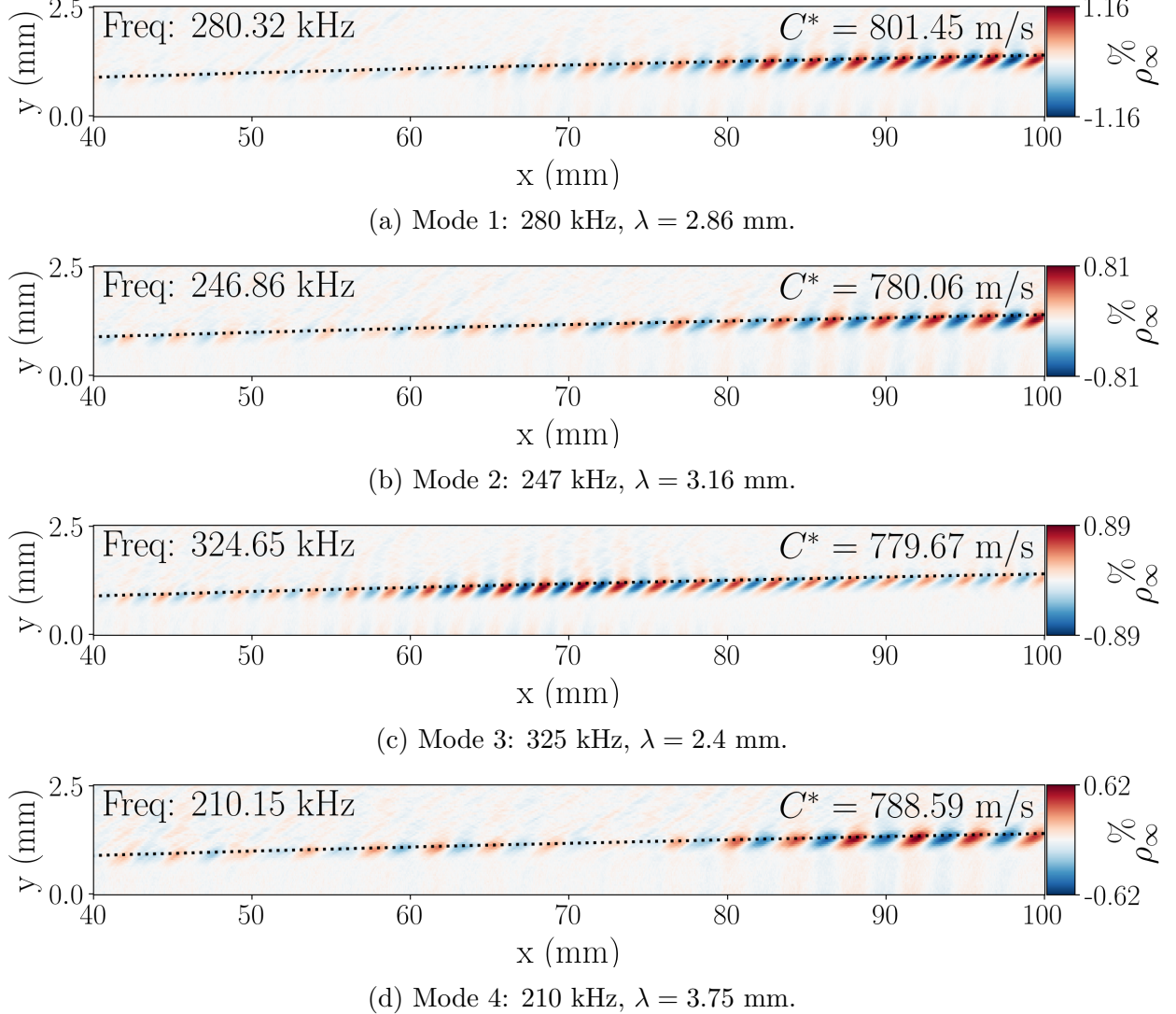


FIG. 12: DMD spatial distribution predictions of the four most energetic modes extracted from unsteady density perturbation snapshots to capture propagating wave characteristics of second-mode disturbances in the hypersonic boundary layer. Mode amplitudes are normalized relative to the most dominant mode and perturbation amplitudes are given as percentages relative to freestream values. Dashed line indicates the boundary-layer edge.

Next we consider in Figure 13 the most energetic DMD modes for the fluctuating components of density ($\tilde{\rho}$), pressure (\tilde{P}), temperature (\tilde{T}), and streamwise velocity (\tilde{U}), all at frequencies close to the dominant second-mode instability of 280 kHz. To facilitate direct comparison with linear stability predictions, DMD analysis results are converted into dimen-

sionless coordinates. The wall-normal coordinate is normalized by the local boundary layer thickness, y/δ , the streamwise position is expressed through the Reynolds number, R (see Eq. 18), frequencies are given as the dimensionless parameter $F = 2\pi w^* \nu^* / U_e^{*2}$, and phase speeds are normalized by the boundary-layer edge velocity, c (see Eq. 7).

The spatial structures of these modes reveal distinct behaviors for each flow variable. For example, the density perturbation, $\tilde{\rho}$ (Fig. 13a), is primarily concentrated within the shear layer near the boundary-layer edge, which is consistent with the PSD profiles in Figs. 10e and 10f. These spatially coherent wave structures captured in the density perturbations are the numerical analogue of the characteristic “rope-like” structures frequently observed in experimental flow visualizations of second-mode instabilities using techniques such as Schlieren imaging [63, 64] and Nanoparticle-tracer based Planar Laser Scattering (NPLS) [65] and the eventual breakdown of these structures is understood to be a key mechanism in the transition to turbulence.

In contrast, the pressure fluctuation, \tilde{P} (Fig. 13b), is most prominent near the wall, below the generalized inflection point, again aligning with our localized PSD simulations (Figs. 10a and 10b). The temperature perturbation, \tilde{T} (Fig. 13c), exhibits a dual-peak structure: a primary peak at the boundary-layer edge and a secondary one near the wall, with a quiet zone around the inflection point, as predicted by LST amplitude functions and consistent with DNS results [66]. Finally, the streamwise velocity perturbation, \tilde{U} (Fig. 13d), is relatively uniform in the wall-normal direction and occurs further upstream, suggesting different dynamics; U -velocity perturbations appear strictly governed by local stability whereas the other variables reflect convective accumulation downstream.

Again, a key characteristic of these traveling waves is their phase speed. The non-dimensional phase speed, c , is calculated by identifying the mode’s wavelength and frequency from DMD (Eq. (7)). For the density, pressure, and temperature modes, the phase speed is approximately $c \approx 0.94$, indicating that these disturbances propagate together as a cohesive acoustic wave packet. The streamwise velocity perturbation, however, travels at a slower phase speed of $c \approx 0.89$, suggesting it may be associated with a different dynamic process, or, a slower-moving component of the second-mode instability.

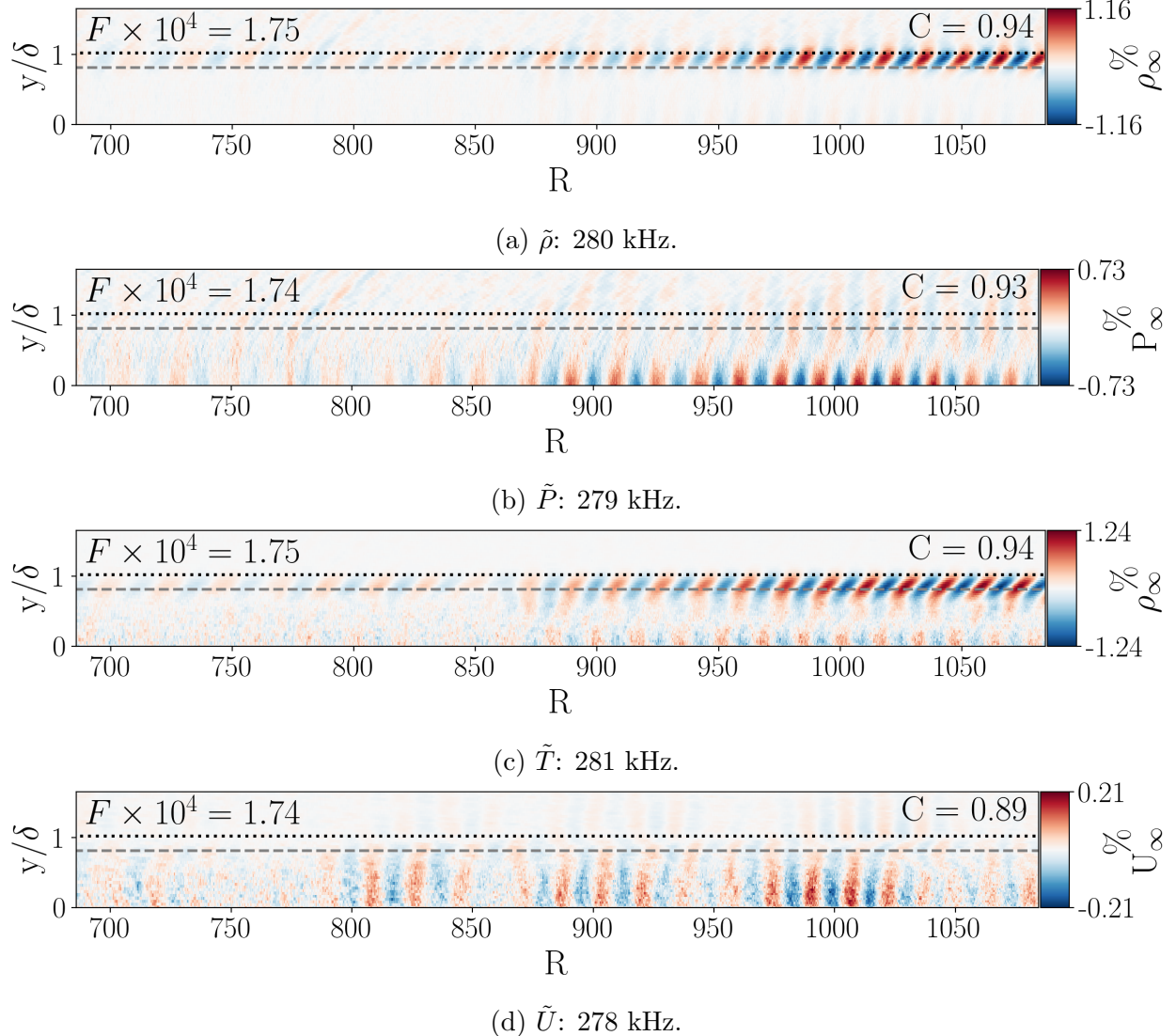


FIG. 13: DMD visualizations of dominant unsteady modes for density, pressure, temperature, and streamwise velocity, highlighting coherent structures near 280 kHz. The non-dimensional phase speed c for $\tilde{\rho}$, \tilde{P} , and \tilde{T} is approximately 0.94; the \tilde{U} mode propagates more slowly at $c \approx 0.89$.

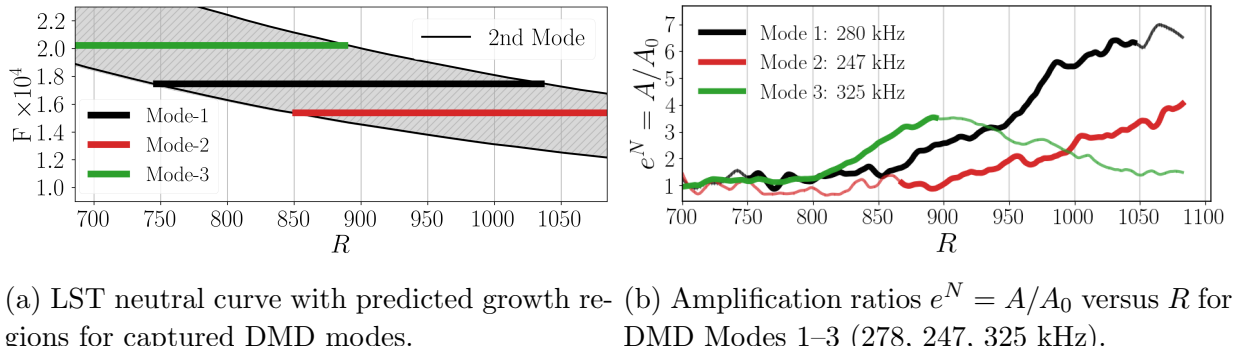
The spatial evolution of each instability wave is quantified via the amplitude (envelope) of the DMD mode. Using Eq. (2), the real-valued amplitude of mode j varies as

$$|\hat{u}_j(\mathbf{x}, \mathbf{y})| = |\hat{u}_j(y)| e^{\sigma_j x}, \quad (23)$$

that is, the oscillatory factor $e^{i\alpha_j x}$ is removed by taking the modulus, leaving the exponential growth/decay governed by σ_j . This isolates the spatial amplification of the disturbance while retaining the wall-normal structure $|\hat{u}_j(y)|$. In what follows we evaluate this envelope along

the boundary-layer edge, from which we extract amplification rates and e^N values within the LST-predicted growth windows.

In Figure 14, the neutral stability curve for our conditions of interest, *i.e.*, the Mach 6 flow over a flat-plate boundary layer is presented, defining the unstable Reynolds number ranges for specific frequencies associated with the DMD modes identified from the numerical simulation. These unstable frequency ranges indicate where perturbations at given frequencies are predicted to amplify according to linear stability theory.



(a) LST neutral curve with predicted growth regions for captured DMD modes. (b) Amplification ratios $e^N = A/A_0$ versus R for DMD Modes 1–3 (278, 247, 325 kHz).

FIG. 14: Linear stability theory neutral curve and DMD mode amplification.

The amplitudes of the DMD modes are depicted in Figs. 15a–15c, with vertical dashed lines marking the theoretically predicted boundaries of the unstable region, which lies between R_{\min} and R_{\max} obtained from Fig. 14a. Examining Mode 1 (280 kHz, Fig. 15a), perturbations demonstrate amplification strictly within the neutral stability boundaries, beginning at $R_{\min} = 744$ and saturating at $R_{\max} = 1038$, after which they decay. For Mode 2 (247 kHz, Fig. 15b), the DSMC/DMD analysis captures only the lower boundary of the unstable region at $R_{\min} = 849$; the predicted upper boundary at $R_{\max} = 1183$ lies beyond the computational domain. For Mode 3 (325 kHz, Fig. 15c), perturbations amplify up to the upper boundary at $R_{\max} = 890$ and then decay.

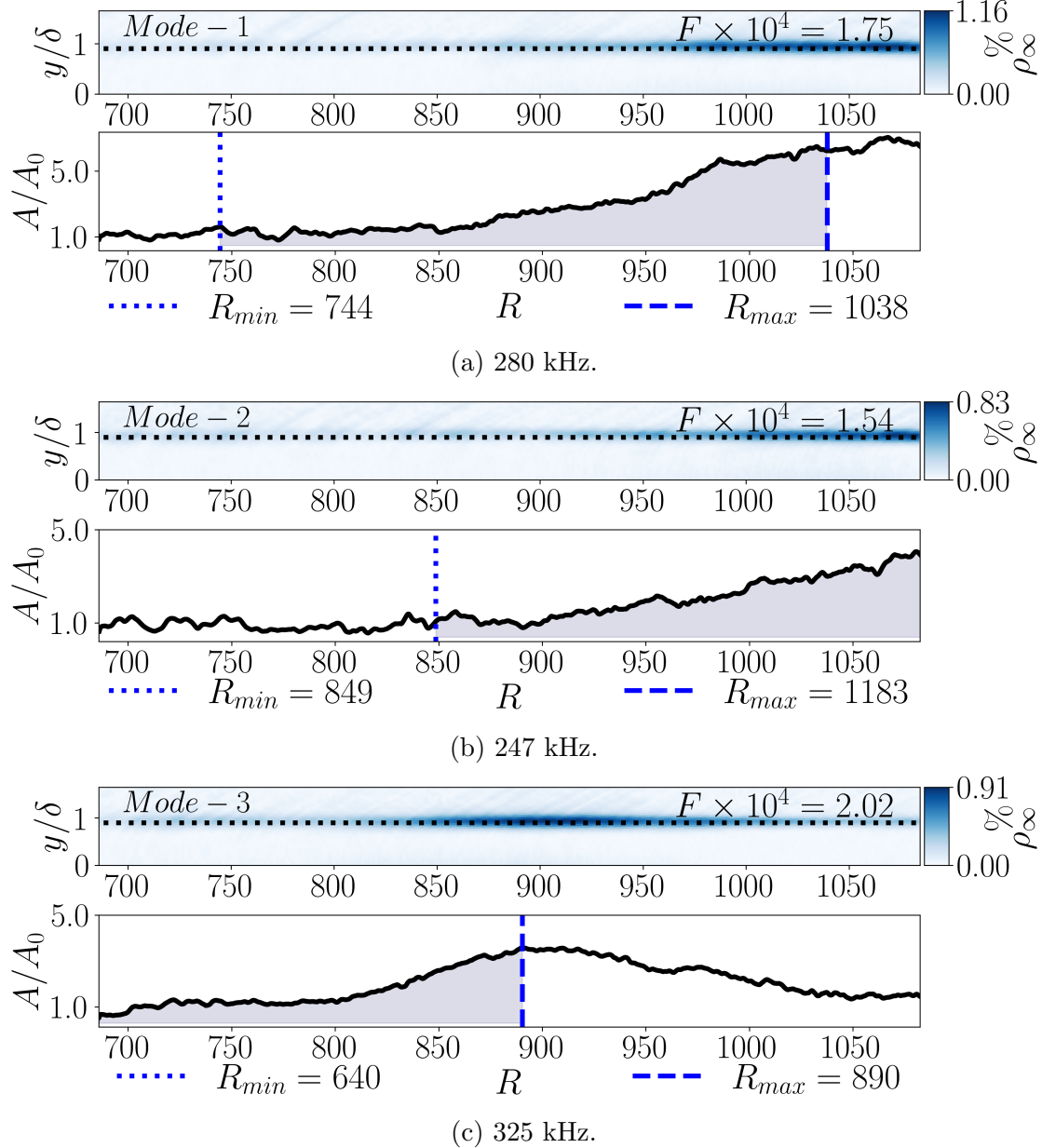


FIG. 15: Spatial structure and amplitude evolution of dominant DMD density modes. For each mode: top panel shows the spatial structure of the density perturbation field across the domain; bottom panel presents the amplitude variation along the boundary-layer edge. Vertical blue lines mark the lower and upper Reynolds number locations of the theoretical amplification window for the respective mode frequencies predicted by LST.

The relative growth rates of these dominant modes, quantified by the amplification factor e^N , are collectively shown in Fig. 15. Amplification of each mode occurs exclusively within its neutral-stability boundaries, followed by decay downstream. Mode 1 at 280 kHz exhibits the largest observed amplification within the computational domain. The maximum amplification observed is about seven, a relatively modest value due to the short streamwise

extent and proximity to the leading edge; larger amplification (and transition) would likely occur over a longer unstable path.

V. EXCITATION OF SECOND MACK MODE INSTABILITIES BY AN ACOUSTIC VIBRATING SURFACE

Having established the ability of DMD using time series data from the kinetic DSMC formulation to model Mack's second mode instabilities in the 100 to 500 kHz region, we now examine how a moving structural surface boundary condition applied to regions of flow over a flat plate will interact with these disturbances. A natural question emerges as to whether these instabilities can be selectively excited or damped in a predictable manner consistent with LST. We consider the harmonic vibrational motion of an AVS[67] as the potential source of interaction with the disturbances discussed in the previous sections. At these high frequencies, the harmonic surface face velocity is expected to be the dominant mechanism in introducing perturbations to the flow, compared to surface deflections. We arrive at this conclusion because the AVS's geometric deflection, being on the order of the flow's mean free path, is unlikely to be perceived by the flow as a significant change in surface position. In contrast, the face velocity of the oscillating AVS influences the flow by altering the velocity of particles due to wall collisions, an effect independent of both the flow's mean free path and the AVS's displacement. For instance, at a frequency of 100 kHz and deflection amplitudes comparable to the mean free path, the resulting harmonic face velocities would be tens of meters per second which will produce particles with new velocities in the tail of thermal distributions at the relatively cold wall temperature of 300 K. Therefore, in the ultrasonic range, the harmonic surface face velocity $\tilde{V}(t)$ is reasoned to play a more dominant role in the fluid-structure interaction than the AVS plate deflection $\tilde{X}(t)$.

The harmonic motion of the AVS can be described by its time-dependent position $\tilde{X}_s(t)$ and velocity $\tilde{V}_s(t)$:

$$\tilde{X}_s(t) = |X_s| \sin(\omega t - \theta), \quad \tilde{V}_s(t) = |V_s| \cos(\omega t - \theta) \quad (24)$$

where $|X_s|$ is the surface deflection amplitude, $|V_s| = \omega|X_s|$ is the surface velocity amplitude, and ω is the angular frequency. The AVS's motion is modeled in the two new DSMC

simulations as an unsteady velocity boundary condition applied at an undeflected surface position of 60 mm from the leading edge, without actually moving the wall panel. The harmonic surface velocity amplitude, $|V_s| = \omega|X_s|$, is set to 100 m/s with a surface plate width of 1 mm and a surface wall temperature and energy accommodation coefficients of 300 K and 1.0. (fully diffuse), respectively are assumed. For the two cases considered, frequencies of 300 and 500 kHz, the face displacement, $|X_s|$ has values of 53 and 31.8 μm , respectively.

As mentioned above, the AVS panel is not actually moved during the DSMC simulation, rather, instead a distribution of normal velocity components of gas particles reflecting from the AVS surface is derived. The analytic expression for the normalized probability distribution function of post-collisional normal velocities for a stationary wall, $F(V_n^*)$, is given by

$$F(V_n^*) = \left(\frac{m}{k_B T_w} \right) V_n^* \exp \left(-\frac{m(V_n^*)^2}{2k_B T_w} \right), \quad 0 < V_n^* < \infty \quad (25)$$

where m is the particle mass, k_B is Boltzmann's constant, T_w is the wall temperature, and V_n^* is the normal velocity of the reflected particles with respect to the wall.

In the case of an AVS, the velocity distributions of the reflected particles are shifted by the AVS's surface velocity at the time of collision giving a new probability distribution of normal velocities V_n' for particles reflecting from a moving wall with surface velocity V_s of

$$F(V_n') = F(V_n^* - V_s^*) \quad (26)$$

$$1 = \int_{V_s^*}^{\infty} F(V_n^* - V_s^*) dV_n \quad (27)$$

While only the normal velocity component is directly altered by the wall interaction, this change modifies the particle speed or its kinetic energy, which is then redistributed throughout the flow via subsequent inter-particle collisions, propagating new AVS disturbances. Appendix VI provides the derivation of an analytic solution for $F(V_n')$ as well as a comparison of how the Maxwellian distribution shifts relative to a non-moving surface. To model this interaction of an AVS time-oscillating wall in DSMC, we adjust the normal velocities of particles reflecting from the wall by the instantaneous velocity of the AVS in its harmonic motion at the moment of collision. The harmonic surface velocity $\tilde{V}(t)$ is utilized where particles reflecting from the surface have their reflected normal velocities altered based on

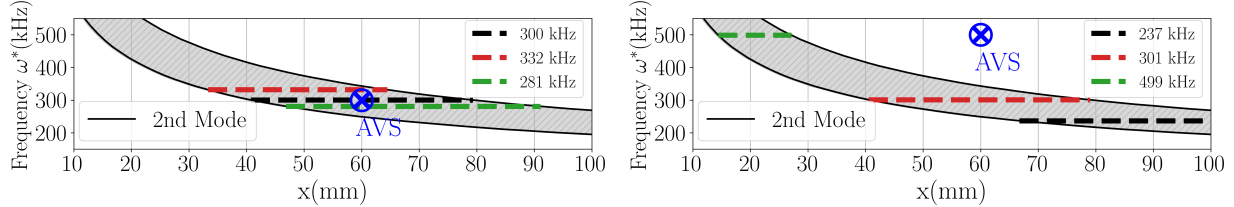
the current velocity of the AVS.

$$V_n^{AVS}(t) = V_n^* + |V_s| \cos\left(\frac{2\pi t}{T} - \theta\right) \quad (28)$$

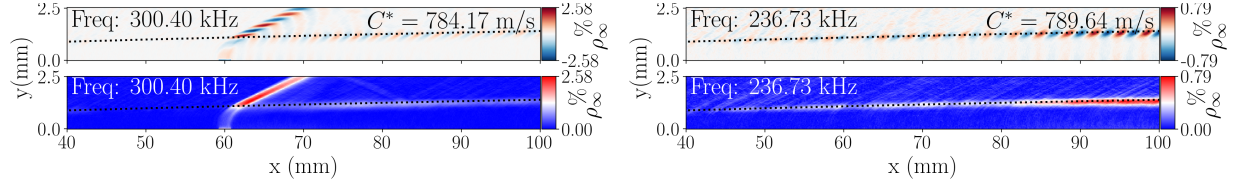
The algorithm is implemented to the DSMC framework, by first sampling the stationary normal velocity V_n^* , corresponding a normal velocity value for a particle reflecting from a stationary wall, and then is shifted by the current face velocity of the AVS which is $|V_s| \cos(\frac{2\pi t}{T} - \theta)$, with this velocity shift depending on the current time t of the DSMC simulation and the period T of the AVS's harmonic motion with its phase θ in time. The phase angle, θ , is presently set to zero for the single-AVS simulations in this study, but provides for future modeling of multiple AVSs.

The first case we consider is an AVS oscillating at 300 kHz, a frequency predicted by LST to fall within the unstable region (Figure 7), thereby amplifying second-mode waves. In contrast, the second case of 500 kHz, lies outside the neutral curve and thus is expected damped instabilities by the flow. The two new DSMC unsteady flowfields were analyzed with DMD for each case. These AVS cases are summarized by amplification windows of the captured DMD modes overlaid on the LST neutral curves, with the 300 kHz AVS lying in the amplification region and the 500 kHz AVS outside it (Figs. 16a and 16b). In both cases, AVS-introduced disturbances are captured within DMD modes at the driving frequency. It is also seen that the flowfield still retains its naturally occurring instabilities captured as DMD modes near 330 and 281 kHz in the 300 kHz case, and near 237 and 301 kHz in the 500 kHz case. This is the expected behavior since the AVS would not alter the boundary layer's profile or any of its intrinsic instability characteristics, where the flow instabilities are expected to be the same as the baseline case.

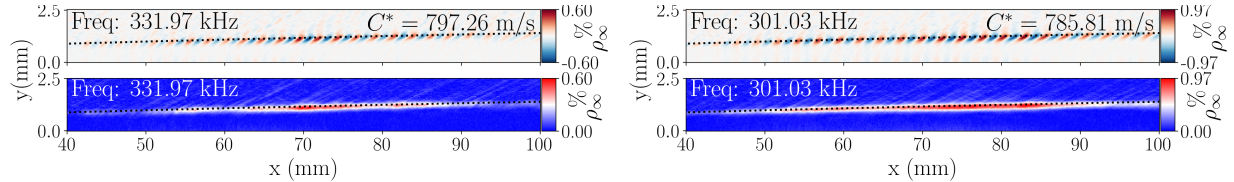
The spatial structures of the most energetic modes are shown in Figs. 16c–16h. For the 300 kHz case, coherent wave structures propagate along the boundary-layer edge and persist downstream, accumulating amplitude as they convect. In contrast, for the 500 kHz case, disturbances are confined to a limited region immediately above the AVS and rapidly decay downstream. Because they fail to establish coherent structures along the shear layer, AVS-introduced perturbations behave consistently with linear stability predictions relative to the baseline flow [1].



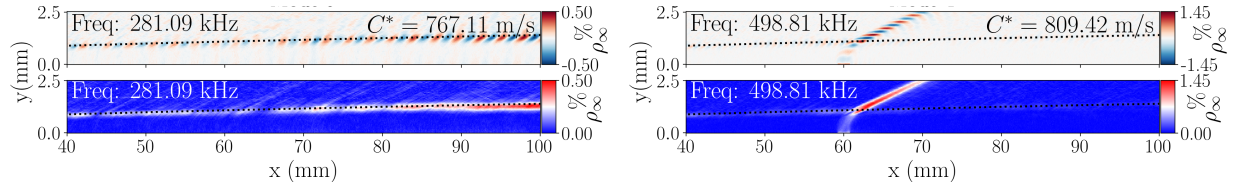
(a) 300 kHz AVS: DMD mode frequencies on LST neutral curve. (b) 500 kHz AVS: DMD mode frequencies on LST neutral curve.



(c) 300 kHz case: AVS-seeded mode also at 300 kHz. (d) 500 kHz case: naturally occurring mode at 237 kHz.



(e) 300 kHz case: naturally occurring mode at 332 kHz. (f) 500 kHz case: naturally occurring mode at 301 kHz.



(g) 300 kHz case: naturally occurring mode at 281 kHz. (h) 500 kHz case: AVS-seeded mode at 498.81 kHz.

FIG. 16: DMD density modes for AVS simulations at 300 and 500 kHz. Left column: 300 kHz AVS case; right column: 500 kHz AVS case. The 300 kHz AVS-seeded mode exhibits coherent wave structures that persist and amplify downstream within the unstable region, while the 500 kHz AVS-seeded mode shows rapid decay.

A more quantitative assessment is provided in Figure 17, which compares the streamwise amplification of the AVS-seeded modes of 300 and 500 kHz versus the baseline, no-AVS case mode (325 kHz). In all cases, peak disturbances are captured above the AVS ($x \approx 60 \text{ mm}$), reflecting the direct influence of the introduced disturbances. However, for the 500 kHz mode, along the shear layer which is the area of interest for the flow instabilities, disturbances decay immediately downstream, confirming stability with respect to this frequency, as predicted

by LST. Conversely, the 300 kHz mode is amplified in the shear layer, from $x = 65$ to 80 mm, during its residence within its unstable region. The baseline 325 kHz case provides the relative amplification factor for disturbances in the non-AVS case.

These results suggest that an AVS could be used to probe and interact with second-mode instabilities in a frequency-selective manner. It should also be noted that, the limited growth in the 300 kHz case is due to the AVS placement deep within the unstable region; *i.e.*, as observed earlier (Figure 9), convective instabilities manifest most prominently downstream of local unstable zones, particularly along the shear layer compared to near-wall regions. A better placement to observe larger growth might be to place the 300 kHz AVS 10 mm upstream of the desired interaction zone, enabling perturbations to accumulate over longer unstable paths. However, this type of analysis is beyond the scope of this work and will be considered in future endeavors.

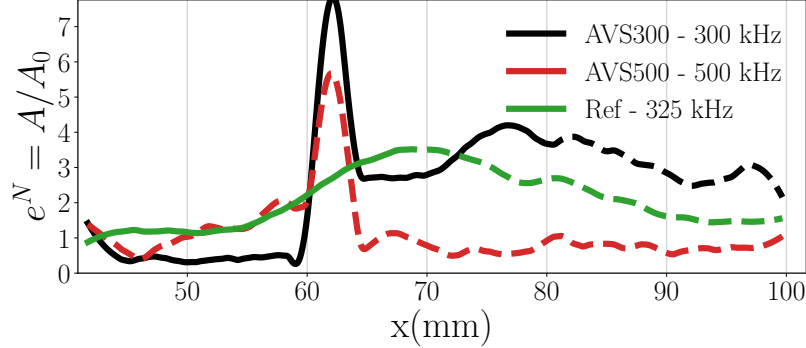


FIG. 17: Streamwise amplification comparison of AVS-seeded modes (300 kHz and 500 kHz) versus baseline (325 kHz).

VI. CONCLUSIONS

In this study, hypersonic boundary-layer instabilities over a flat plate were investigated using the particle-kinetic DSMC method coupled with data-driven DMD analyses. Using a slip-flow correction to the compressible flat-plate boundary layer solutions, data probes were placed in along and across the shear layer at strategic locations. It was observed that the DSMC-simulated flowfield naturally developed second Mack mode instabilities without any external seeding, *i.e.*, arising spontaneously from intrinsic simulation noise. Frequencies of these perturbations, captured via local PSD analysis, were found to fall within the range predicted by linear stability theory. Notably, perturbations measured near the sur-

face remain strictly within locally unstable regions inside the neutral curves, whereas those along the boundary-layer edge obtain their peak amplitudes just downstream of the unstable growth region, indicating that these instabilities are amplified and accumulate as they convect downstream. For a more thorough examination, the time-accurate unsteady DSMC flowfield snapshots were analyzed using DMD to extract global spatial structures of the instability waves at the frequencies identified in the PSD spectra. We show that DMD breaks down second Mack mode instabilities into their individual constituent waves. An N-factor analysis of these DMD modes confirms that for each of the captured modes, growth occurs solely in their respective unstable regions predicted by linear stability theory. This verifies that the DMD modes are indeed the decomposed structures of second-mode wave packets.

With the demonstration of the ability of combined DSMC and DMD approaches to model second mode Mack instabilities, we investigated the possible interactions of an AVS to selectively grow or quench hypersonic boundary layer disturbances in the 100 to 500 kHz range. An efficient approach to model the interaction of the AVS with the boundary layer flow was developed by modifying the scattered particle velocity distribution function, instead of actually moving the surface. An AVS oscillating at a frequency within the locally unstable region, even at minimal deflection amplitudes, was shown to successfully interact with boundary-layer instabilities, introducing perturbations that persist and amplify in the predicted growth zone and decay thereafter. In contrast, an AVS at a stable-region frequency generated perturbations that dissipated immediately without sustained propagation.

Overall, the present study shows that the DSMC method, integrated with data-driven techniques, offers a robust approach not only for investigating unsteady hypersonic boundary layer flows in the context of second Mack mode instabilities. We demonstrate the continued improvement in DSMC algorithms that enable us to model an exceptionally high, for a particle kinetic method, number density of $1.2 \times 10^{24} \text{ m}^{-3}$. While such conditions correspond to a low Reynolds number from a continuum perspective, they represent the state of the art for DSMC. Furthermore, the implementation of a simple AVS introduces the first attempt to model fluid-structure interactions from a purely kinetic point of view.

ACKNOWLEDGMENTS

This work was supported by the Office of Naval Research under Grant No. N00014-23-1-2839, "Kinetic Treatment of Sources and Mechanisms that Drive Unsteady, Shock-dominated Flow Instability" (Program Officer: Dr. Eric Marineau). Computational resources were provided by the Texas Advanced Computing Center (TACC) at the University of Texas, using the Frontera supercomputer (Project No. CTS23002), funded by the National Science Foundation (NSF).

APPENDIX A: DERIVATION OF PARTICLE SPEED DISTRIBUTION FOR MOVING WALL

To find the speed probability distribution of particles reflected from a moving surface, we start with the initial integral:

$$1 = \int_{-\infty}^{\infty} \int_{-\infty}^{\infty} \int_A^{\infty} f(V_x) f(V_y) f(V_N) dV_x dV_y dV_N \quad (29)$$

where $f(V_x)$, $f(V_y)$, and $f(V_N)$ are the probability distribution functions for the velocities in the x, y, and face normal directions, respectively. The distribution functions are defined as:

$$f_t(V_{x,y}) = \sqrt{\frac{m}{2\pi kT}} \exp\left(-\frac{m}{2kT} V_{x,y}^2\right) \quad (30) \quad f_n(V_N) = \frac{m}{kT} V_N \exp\left(-\frac{m}{2kT} V_N^2\right) \quad (31)$$

where $f_t(V_{x,y})$ describes the tangential velocity components and $f_n(V_N)$ describes the normal velocity. Rewriting the initial integral using these distribution functions, we have:

$$1 = \int_{-\infty}^{\infty} \int_{-\infty}^{\infty} \int_A^{\infty} \frac{1}{(2\pi)} \left(\frac{m}{kT}\right)^2 V_N \exp\left(-\frac{m}{2kT}(V_x^2 + V_y^2)\right) \exp\left(-\frac{m}{2kT} V_N^2\right) dV_x dV_y dV_N \quad (32)$$

Next, we express the speed probability distribution as:

$$1 = \int_0^{\infty} f(C) dC \quad \text{where} \quad C = \sqrt{V_x^2 + V_y^2 + V_N^2} \quad (33)$$

Transforming coordinates from Cartesian to spherical, we get:

$$dV = dV_x dV_y dV_N \rightarrow dV = C^2 \cos \theta d\theta d\psi dC \quad (34)$$

The volume element in spherical coordinates is thus transformed as shown above. For a full Maxwellian distribution, we rewrite the integral:

$$1 = \int_{-\infty}^{\infty} \int_{-\infty}^{\infty} \int_{-\infty}^{\infty} f(V_x) f(V_y) f(V_N) dV_x dV_y dV_N \rightarrow \int_0^{2\pi} \int_0^{\frac{\pi}{2}} \int_0^{\infty} f(C) dC d\theta d\psi \quad (35)$$

This shows the transformation of the integral limits and the inclusion of the spherical coordinate system.

The normal velocity distribution function is shifted for the reflected particles:

$$f_N(V_N^*) = f_N(V_N - A) \quad (36)$$

Where V_N^* is the normal velocities of the particle reflecting from a moving surface. This shift indicates that the velocities of the reflected particles are shifted right by A in their probability distributions. The corresponding integral now becomes:

$$1 = \int_{-\infty}^{\infty} \int_{-\infty}^{\infty} \int_A^{\infty} f(V_x) f(V_y) f(V_N - A) dV_x dV_y dV_N \quad (37)$$

which will be:

$$1 = \int_{-\infty}^{\infty} \int_{-\infty}^{\infty} \int_A^{\infty} \frac{1}{2\pi} B^2 (V_N - A) e^{-\frac{1}{2}B(V_y^2 + V_z^2 + (V_N - A)^2)} dV_y dV_z dV_N \quad (38)$$

where $B = \frac{m}{kT}$. Now, performing the transformation to the spherical coordinate system, the integral then becomes:

$$1 = \int_0^{2\pi} \int_{\theta_{min}}^{\frac{\pi}{2}} \int_0^{\infty} B^2 (C \sin \theta - A) \exp\left(-\frac{B}{2}(C^2 - 2CA \sin \theta + A^2)\right) C^2 \cos \theta dC d\theta d\psi \quad (39)$$

where $\theta_{min} = \arcsin\left(\frac{A}{C}\right)$. Simplifying the integral for $B = \frac{m}{kT}$ we have:

$$f(C) = C \exp\left(-\frac{B}{2}(C^2 + A^2)\right) \left[\frac{\exp(ABC(ABC - A^2B - 1)) + \exp(A^2B)}{A^2} \right] \quad (40)$$

where $f(C) dC$ represents the speed probability distribution of the particles reflecting from a moving wall with positive velocity A in the wall normal direction.

$$1 = \int_A^{\infty} f(C) dC \quad (41)$$

While only the normal velocity component is directly altered by the wall interaction, this change modifies the total particle speed. The particle speed is a direct measure of its kinetic energy, and this energy is then redistributed throughout the flow via subsequent

inter-particle collisions, propagating the disturbance introduced by the AVS. The particle speed C is defined as: $C = \sqrt{(V_x^*)^2 + (V_y^*)^2 + (V_n^{AVS})^2}$ where V_x^* and V_y^* are the tangential velocity components and V_n^{AVS} is the normal velocity component altered by the presence of the AVS (see Eq. (28)). The resultant speed probability distribution function for particles reflecting from a moving wall takes the following form:

$$1 = \int_{\max(V_s^*, 0)}^{\infty} f(C) dC \quad (42)$$

$$f(C) = \begin{cases} \frac{C}{V_s^{*2}} \exp\left(-\frac{B}{2}(C^2 + V_s^{*2})\right) \\ \quad \times \left(\exp(BV_s^*C)(BV_s^*C - V_s^{*2}B - 1) + \exp(V_s^{*2}B) \right) & C \geq |V_s^*| \\ \frac{C}{V_s^{*2}} \exp\left(-\frac{B}{2}(C^2 + V_s^{*2})\right) \\ \quad \times \left(\exp(BV_s^*C)(BV_s^*C - V_s^{*2}B - 1) \right. \\ \quad \left. + \exp(-BV_s^*C)(BV_s^*C + V_s^{*2}B + 1) \right) & C < |V_s^*| \end{cases} \quad (43)$$

where C is the particle speed and V_s^* is the face velocity of the wall and $B = \frac{m}{kT}$, see the Appendix in Sec VI where the derivation of Eq. 43 for positive surface velocities case is provided. In the limit that $V_s^* = 0$, Eq. 43 becomes:

$$F(C) = \frac{1}{2} \left(\frac{m}{k_B T_w} \right)^2 C^3 \exp\left(-\frac{mC^2}{2k_B T_w}\right), \quad 0 < C < \infty \quad (44)$$

Which is the well known "Half-Maxwellian" distribution, corresponding to the probability distribution of particle speeds reflected from a stationary wall.

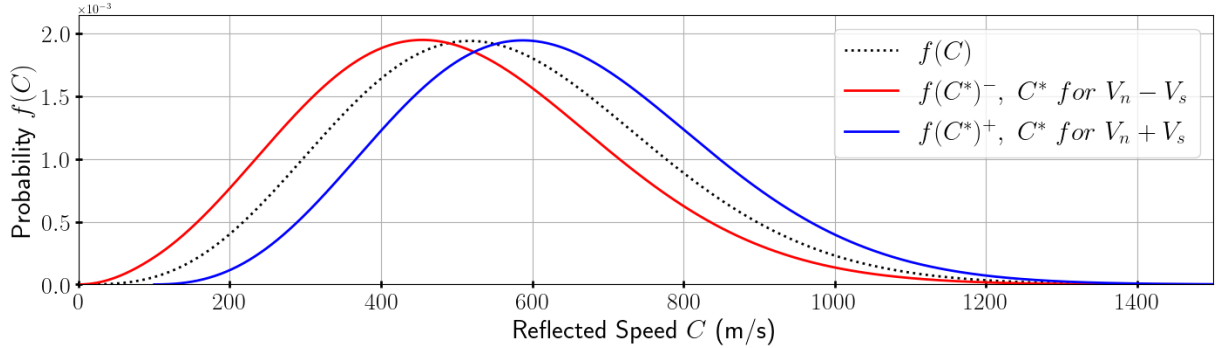


FIG. 18: Probability distributions of reflected particle Speeds, wall temperature of 300K, with 100m/s face velocity

For an AVS with a harmonic face velocity $|V_s| = 100 \text{ m/s}$ and a surface temperature of 300K, Fig. 18 shows the range of speed distributions for particles reflecting off this vibrating surface. The harmonic face velocity of the AVS, with a 100 kHz oscillation frequency, introduces statistically significant changes in the overall reflected particle speed distributions. These speed distributions will no longer be steady, and instead, will fluctuate in time due to the AVS's motion. This unsteadiness in particle speeds will propagate throughout the flow via subsequent particle collisions, driving the fluid-structure interaction.

[1] L. M. Mack, *Boundary-Layer Linear Stability Theory*, AGARD Report 709 (AGARD, Neuilly-sur-Seine, France, 1984).

[2] A. Fedorov, Transition and stability of high-speed boundary layers, *Annual Review of Fluid Mechanics* **43**, 79 (2011).

[3] A. Demetriades, An experiment on the stability of hypersonic laminar boundary layers, *Journal of Fluid Mechanics* **7**, 385 (1960).

[4] K. F. Stetson, *Hypersonic Boundary-Layer Transition Experiments*, Technical Report AFWAL-TR-80-3062 (Air Force Wright Aeronautical Laboratories, Wright-Patterson AFB, OH, 1980).

[5] Kenneth F. Stetson, K. F. Stetson, Roger L. Kimmel, and R. L. Kimmel, Example of Second-Mode Instability Dominance at a Mach Number of 5.2, *AIAA Journal* **30**, 2974 (1992), mAG ID: 2019974634.

[6] M. V. Morkovin, Recent insights into instability and transition to turbulence in open-flow

systems, NASA Contract Nos. NAS1-18107 and NAS1-18605, ICASE, NASA Langley Research Center (1988).

- [7] M. Malik, Numerical methods for hypersonic boundary layer stability, *Journal of Computational Physics* **86**, 376 (1990).
- [8] M. P. Juniper, A. Hanifi, and V. Theofilis, Modal Stability Theory, *Applied Mechanics Reviews* **66**, 024804 (2014).
- [9] T. Herbert, Parabolized stability equations, *Annual Review of Fluid Mechanics* **29**, 245 (1997).
- [10] S. P. Schneider, Flight Data for Boundary-Layer Transition at Hypersonic and Supersonic Speeds, *Journal of Spacecraft and Rockets* **36**, 8 (1999).
- [11] S. P. Schneider, Hypersonic laminar–turbulent transition on circular cones and scramjet forebodies, *Progress in Aerospace Sciences* **40**, 1 (2004).
- [12] T. J. Juliano, S. P. Schneider, D. C. Berridge, M. A. Kegerise, and B. M. Wheaton, Measurements and computations of second-mode instability waves in three hypersonic wind tunnels, in *48th AIAA Aerospace Sciences Meeting Including the New Horizons Forum and Aerospace Exposition*, AIAA 2010-5002 (Orlando, Florida, 2010).
- [13] C. R. Alba, K. M. Casper, S. J. Beresh, S. P. Schneider, and D. C. Berridge, Comparison of experimentally measured and computed second-mode disturbances in hypersonic boundary-layers, in *48th AIAA Aerospace Sciences Meeting Including the New Horizons Forum and Aerospace Exposition*, AIAA 2010-897 (Orlando, Florida, 2010).
- [14] E. C. Marineau, C. G. Moraru, D. R. Lewis, J. D. Norris, J. F. Lafferty, T. P. Wadhams, and J. A. Long, First and fifth hypersonic international flight research experimentation’s flight and ground tests, *Journal of Spacecraft and Rockets* **56**, 421 (2020).
- [15] R. E. Kennedy, J. S. Jewell, P. Paredes, and S. J. Laurence, Characterization of instability mechanisms on sharp and blunt slender cones at Mach 6, *Journal of Fluid Mechanics* **936**, A39 (2022).
- [16] Q. Tang, Y. Zhu, X. Chen, and C. Lee, Development of second-mode instability in a Mach 6 flat plate boundary layer with two-dimensional roughness, *Physics of Fluids* **27**, 064105 (2015).
- [17] H. S. Ribner, *Convection of a Pattern of Vorticity Through a Shock Wave*, Technical Note 2864 (NACA, 1953).
- [18] H. S. Ribner, *Convection of a Pattern of Vorticity Through a Shock Wave*, Report 1164

(NACA, 1954).

- [19] F. K. Moore, *Unsteady Oblique Interaction of a Shock Wave with a Plane Disturbance*, Technical Note 2879 (NACA, 1953).
- [20] F. K. Moore, *Unsteady Oblique Interaction of a Shock Wave with a Plane Disturbance*, Report 1165 (NACA, 1954).
- [21] J. McKenzie and K. Westphal, Interaction of linear waves with oblique shock waves, *The Physics of Fluids* **11**, 2350 (1968).
- [22] A. Fedorov and A. Tumin, Receptivity of high-speed boundary layers to kinetic fluctuations, *AIAA Journal* **55**, 2335 (2017).
- [23] X. Zhong and Y. Ma, Boundary-layer receptivity of Mach 7.99 flow over a blunt cone to free-stream acoustic waves, *Journal of Fluid Mechanics* **556**, 55 (2006).
- [24] R. Bhaskaran, K. J. Franko, and S. K. Lele, Direct numerical simulation of transition and heat transfer overshoot in a mach 6 flat plate boundary layer, in *41st AIAA Fluid Dynamics Conference and Exhibit*, AIAA 2011-3874 (Honolulu, Hawaii, 2011).
- [25] J. Sivasubramanian and H. F. Fasel, Direct numerical simulation of laminar-turbulent transition in a hypersonic boundary layer on a sharp cone, in *AIAA Scitech 2019 Forum*, AIAA 2019-0276 (San Diego, California, 2019).
- [26] P. Paredes, M. M. Choudhari, and F. Li, Blunt-body paradox and improved application of transient-growth framework, *AIAA Journal* **56**, 2604 (2018).
- [27] P. Paredes, M. M. Choudhari, F. Li, J. S. Jewell, and R. L. Kimmel, Nonmodal growth of traveling waves on blunt cones at hypersonic speeds, *AIAA Journal* **57**, 4738 (2019).
- [28] A. Batista, A. A. Khan, and J. Kuehl, On the mechanism by which nose bluntness suppresses second-mode instability, *Theoretical and Applied Mechanics Letters* **10**, 230 (2020).
- [29] I. T. Karpuzcu and D. A. Levin, Loss of axial symmetry in hypersonic flows over conical shapes, *Physical Review Fluids* **10**, 033901 (2025).
- [30] M. Goldstein, The evolution of tollmien–scliching waves near a leading edge, *Journal of Fluid Mechanics* **127**, 59 (1983).
- [31] F. Smith, On the first-mode instability in subsonic, supersonic or hypersonic boundary layers, *Journal of Fluid Mechanics* **198**, 127 (1989).
- [32] M. Goldstein and P. Ricco, Non-localized boundary layer instabilities resulting from leading edge receptivity at moderate supersonic mach numbers, *Journal of Fluid Mechanics* **838**, 435

(2018).

- [33] X. Zhong and X. Wang, Direct Numerical Simulation on the Receptivity, Instability, and Transition of Hypersonic Boundary Layers, *Annual Review of Fluid Mechanics* **44**, 527 (2012).
- [34] X. Li, D. Fu, and Y. Ma, Direct numerical simulation of hypersonic boundary-layer transition over a blunt cone with a small angle of attack, *Physics of Fluids* **22**, 025105 (2010).
- [35] H. Goparaju and D. V. Gaitonde, Role of entropic instabilities in laminar-turbulent transition on a blunted flat plate, *Physical Review Fluids* **7**, 103901 (2022).
- [36] C. Wang, J. Ou, and J. Chen, Rarefaction effects on hypersonic boundary-layer stability over a blunt cone at varying degrees of wall cooling and nose bluntness in near-continuum regime, *Physical Review Fluids* **10**, 093901 (2025).
- [37] A. Beskok and G. E. Karniadakis, Report: a model for flows in channels, pipes, and ducts at micro and nano scales, *Microscale thermophysical engineering* **3**, 43 (1999).
- [38] S. S. Sawant, V. Theofilis, and D. Levin, On the synchronisation of three-dimensional shock layer and laminar separation bubble instabilities in hypersonic flow over a double wedge, *Journal of Fluid Mechanics* **941**, A7 (2022).
- [39] G. A. Bird, *Molecular Gas Dynamics and the Direct Simulation of Gas Flows* (Oxford University Press, Oxford, UK, 1994).
- [40] S. F. Gimelshein and I. J. Wysong, Nonequilibrium air flow predictions with a high-fidelity direct simulation Monte Carlo approach, *Physical Review Fluids* **4**, 033405 (2019).
- [41] I. T. Karpuzcu, M. P. Jouffray, and D. A. Levin, Collisional Radiative Modeling of Electronically Excited States in a Hypersonic Flow, *Journal of Thermophysics and Heat Transfer* **36**, 982 (2022).
- [42] R. M. McMullen, M. C. Krygier, J. R. Torczynski, and M. A. Gallis, Navier-Stokes Equations Do Not Describe the Smallest Scales of Turbulence in Gases, *Physical Review Letters* **128**, 114501 (2022).
- [43] O. Tumuklu, D. A. Levin, and V. Theofilis, Modal analysis with proper orthogonal decomposition of hypersonic separated flows over a double wedge, *Physical Review Fluids* **4**, 033403 (2019).
- [44] I. T. Karpuzcu and D. A. Levin, Study of side-jet interactions over a hypersonic cone flow using kinetic methods, *AIAA Journal* **61**, 4741 (2023), <https://doi.org/10.2514/1.J063020>.
- [45] A. Klothakis, H. Quintanilha, S. S. Sawant, E. Protopapadakis, V. Theofilis, and D. A. Levin,

Linear stability analysis of hypersonic boundary layers computed by a kinetic approach: A semi-infinite flat plate at $\mathrm{M}_\infty \leq 9$, *Theoretical and Computational Fluid Dynamics* **36**, 117 (2022).

[46] S. A. A. Hasnine, V. Russo, A. Tumin, and C. Brehm, Biorthogonal decomposition of the disturbance flow field generated by particle impingement on a hypersonic boundary layer, *Journal of Fluid Mechanics* **969**, A1 (2023).

[47] P. J. Schmid, Dynamic mode decomposition of numerical and experimental data, *Journal of Fluid Mechanics* **656**, 5 (2010).

[48] I. T. Karpuzcu, M. Senkardesler, and D. A. Levin, On flow unsteadiness in strongly separated high-speed ramp flows using kinetic and data-driven methods, *Physics of Fluids* **37**, 096136 (2025).

[49] F. Gómez, S. L. Clainche, P. Paredes, M. Hermanns, and V. Theofilis, Four Decades of Studying Global Linear Instability: Progress and Challenges, *AIAA Journal* **50**, 2731 (2012).

[50] G. A. Bird, in *Molecular Gas Dynamics and the Direct Simulation of Gas Flows* (Clarendon, Oxford, England, U.K., 1994).

[51] O. Tumuklu, V. Theofilis, and D. A. Levin, On the unsteadiness of shock laminar boundary layer interactions of hypersonic flows over a double cone, *Physics of Fluids* **30**, 106111 (2018).

[52] M. S. Ivanov and S. V. Rogasinsky, Analysis of the numerical techniques of the direct simulation Monte Carlo method in the rarefied gas dynamics, *Soviet Journal of Numerical Analysis and Mathematical Modeling* **3**, 453 (1988).

[53] M. Ivanov, A. Kashkovsky, S. Gimelshein, G. Markelov, A. Alexeenko, Y. Bondar, G. Zhukova, S. Nikiforov, and P. Vaschenkov, Smile system for 2d/3d dsmc computations, in *Proceedings of 25th International Symposium on Rarefied Gas Dynamics* (Novosibirsk Publ. House of the Siberian Branch of the Russian Academy of Sciences, St. Petersburg, Russia, 2007) pp. 21–28.

[54] O. T. Schmidt and T. Colonius, Guide to spectral proper orthogonal decomposition, *AIAA Journal* **58**, 1023 (2020).

[55] P. Chambre and S. Schaaf, *Flow of Rarefied Gases*, Princeton Legacy Library (Princeton University Press, 2017).

[56] E. R. Van Driest, Investigation of laminar boundary layer in compressible fluids using the crocco method, *NACA TN 2579* (1952).

[57] L. M. Mack, On the inviscid acoustic-mode instability of supersonic shear flows: Part 1:

Two-dimensional waves, *Theoretical and Computational Fluid Dynamics* **2**, 97 (1990).

[58] S. Özgen and S. A. Kircali, Linear stability analysis in compressible, flat-plate boundary-layers, *Theoretical and Computational Fluid Dynamics* **22**, 1 (2008).

[59] P. Welch, The use of fast fourier transform for the estimation of power spectra: A method based on time averaging over short, modified periodograms, *IEEE Transactions on Audio and Electroacoustics* **15**, 70 (1967).

[60] P. Virtanen, R. Gommers, and T. Oliphant, Scipy 1.0: fundamental algorithms for scientific computing in python (2020).

[61] D. Gai and W. Cao, Stability and transition for long-duration hypersonic flat-plate boundary layer considering wall thermal effect, *Physics of Fluids* **37**, 064104 (2025).

[62] A. C. Ghannadian, R. C. Gosse, S. Roy, Z. D. Lawless, S. A. Miller, and J. S. Jewell, Spatiotemporal koopman decomposition of second mode instability from a hypersonic schlieren video, *Physics of Fluids* **36**, 096118 (2024).

[63] N. J. Parziale, J. E. Shepherd, and H. G. Hornung, Observations of hypervelocity boundary-layer instability, *Journal of Fluid Mechanics* **781**, 87 (2015).

[64] S. A. Miller, J. J. Redmond, K. Jantze, C. Scalo, and J. S. Jewell, Investigation of second-mode instability attenuation over porous materials in mach-6 quiet flow, in *AIAA AVIATION 2022 Forum*, AIAA 2022-3530 (2022).

[65] B. Zhang, S. Yi, H. Niu, X. Liu, X. Lu, and L. He, Effect of reynolds number on second-mode waves in transitional hypersonic boundary layers, *Experimental Thermal and Fluid Science* **141**, 110786 (2023).

[66] O. M. Browne, A. P. Haas, H. F. Fasel, and C. Brehm, An efficient linear wavepacket tracking method for hypersonic boundary-layer stability prediction, *Journal of Computational Physics* **380**, 243 (2019).

[67] R. Zhao, C. Wen, Y. Zhou, G. Tu, and J. Lei, Review of acoustic metasurfaces for hypersonic boundary layer stabilization, *Progress in Aerospace Sciences* **130**, 100808 (2022).